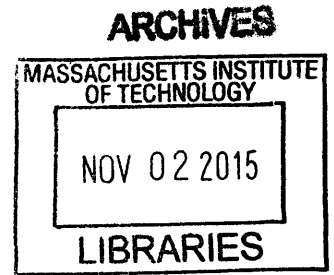


Towards Infrared Plasmonics in Graphene

by

Cheng Peng

B.A., Cornell University (2013)



Submitted to the Department of Electrical Engineering and Computer Science

in partial fulfillment of the requirements for the degree of

Master of Science in Electrical Engineering and Computer Science

at the

MASSACHUSETTS INSTITUTE OF TECHNOLOGY

September 2015

© Massachusetts Institute of Technology 2015. All rights reserved.

Signature redacted


Author
Department of Electrical Engineering and Computer Science
August 28, 2015

Signature redacted

Certified by...

Dirk R. Englund
Assistant Professor
Thesis Supervisor

Signature redacted

Accepted by....

Leslie A. Kolodziejski
Chairman, Department Committee on Graduate Theses

Towards Infrared Plasmonics in Graphene

by

Cheng Peng

Submitted to the Department of Electrical Engineering and Computer Science
on August 28, 2015, in partial fulfillment of the
requirements for the degree of
Master of Science in Electrical Engineering and Computer Science

Abstract

Graphene plasmons have recently been proposed as an alternative to noble-metal plasmons in the field of photonics, due to its extremely tight light confinement, relatively long-lived collective oscillation, and high tunability via electrostatic gating. Successful support and tuning of graphene plasmonic modes rely on controllable doping of graphene to high carrier densities in nanometer-scale structures. In this thesis, an experimental approach to generating nanoscale spatial carrier density modulation of graphene using electrolyte gates and crosslinked-PMMA screen is proposed and investigated. The increased optical absorption in the infrared region due to plasmon resonances induced by the proposed scheme is numerically studied. We then present the fabrication technique of the proposed scheme for various nanostructure geometries. Finally, we provide an outlook of future studies of graphene plasmonics, including plasmon excitation with solid-state cavity quantum electrodynamics (QED).

Thesis Supervisor: Dirk R. Englund

Title: Assistant Professor, Department of Electrical Engineering and Computer Science

Acknowledgments

First of all I would like to thank my advisor Professor Dirk Englund for introducing me to the exciting field of graphene optoelectronics and plasmonics. Thanks also for always being willing to discuss problems coming up in experiments and for constantly providing me with suggestions for new directions to pursue. Next I would like to thank Ren-Jye for supervising me and helping me with any problems I have in both graphene theory and experiments since I joined the group. Thanks for teaching me most of what I know about optics and optoelectronic experiments. I would also like to thank Dmitri for supervising and working with me on this graphene plasmonics project, and for teaching me very useful condensed matter theory and experience of doing experiments bit by bit. I learn a great deal from his broad knowledge of physics and his way of performing research.

My next block of thanks goes to my colleagues in Quantum Photonics Group who have spent the last two years with me in the EECS program: in particular, Michael, Mihir, Jeff, Carson, Darius, and Jordan. Thanks for all the meaningful discussions both in optics and physics and outside research, and for all the pleasant time spent together both in the lab and outside.

Last but not least I would want to thank my parents and my brother Yachi. Without their constant and unconditional support this work could not have been possible.

Contents

1	Introduction	15
1.1	Overview of graphene properties	16
1.2	Graphene surface-plasmon-polaritons (SPP)	19
1.2.1	Graphene plasmonic mode dispersion	20
2	Enhanced optical absorption with confined graphene plasmons in nanostructures	23
2.1	Plasmons in graphene nanodisks	25
2.2	Enhanced optical absorption with periodic nanostructures in graphene	28
2.2.1	Universal limit to absorption in thin films - an overview	30
2.2.2	Periodic nanodisk arrays in patterned graphene	31
2.2.3	Periodic nanohole(antidisk) arrays in patterned graphene	33
2.2.4	Periodic nanoscale conductivity modulation in extended graphene	36
3	Nanoscale carrier density modulation of graphene with electrolyte gates and crosslinked-PMMA screens	41
3.1	Electrolytic gating of graphene	42
3.2	Nanoscale electrolyte gates with electrolyte-PMMA-screen geometry	44
3.3	Proof-of-principle testings of electrolyte-PMMA-screen gates	46
3.3.1	Protection from charge leaking through PMMA screens	47
3.3.2	Resistance measurement of a graphene p - n junction	49
3.3.3	Photocurrent measurement of a series of graphene p - n junctions	51
3.4	Fabrication technique for electrolyte-PMMA-screen gates	54

3.4.1	Large-scale fabrication procedures	54
3.4.2	Graphene devices with nanoscale carrier density modulation gates	55
4	Conclusion and outlook	57

List of Figures

1-1 Graphene’s lattice structure in momentum-space and graphene’s electronic band structure (Dirac cones) at K and K’ points. From [1]. . . 17

1-2 Characteristics of optical absorption in graphene. (a) A typical absorption spectrum of graphene. (b) Illustration of various optical transition processes. From [39]. 18

1-3 (a) Plasmon dispersion of graphene calculated within Random Phase Approximation. Black dash line indicates plasmon dispersion in the long wavelength and high doping limit. Gray shades indicate regions where Landau damping from electron-hole pair excitations becomes prominent. From [30]. (b) Plasmon dispersion of graphene measured using Electron Energy Loss Spectroscopy (EELS) with graphene on SiC. From [38]. 21

2-1	Experimental observation of graphene surface plasmons in patterned graphene micro/nanostructures. (a) Schematic diagram of patterned graphene nanodisk arrays on top of an ITO-coated silica substrate. (b) Experimental and theoretical extinction spectra for fixed doping of graphene nanodisks ($E_F = 0.61$ eV) and varying disk diameter (50 - 190 nm). The extinction is given in difference percentage between regions with and without graphene. (c) AFM images of patterned graphene microribbons with varying width (1 - 4 μm). (d) Change of transmission spectra with different graphene microribbon widths for the same doping concentration of $1.5 \times 10^{13} \text{cm}^{-2}$. All spectra were normalized by their respective peak values for convenience of comparison. (a)(b) from [18]; (c)(d) from [33].	24
2-2	Extinction cross section of a doped graphene nanodisk normalized to the geometrical area of the disk, showing a prominent resonance characteristic of a dipolar plasmon excited in the nanodisk. Parameters used in the simulation: disk radius $r = 50$ nm, Fermi level $E_F = 0.5$ eV, and mobility $\mu = 10000$ cm^2/Vs	26
2-3	Scattered electric field intensity around a graphene nanodisk corresponding to a graphene plasmonic disk mode at 7 μm , normalized to the field intensity without any graphene. Light is incident perpendicular to the disk plane (xy-plane), linearly polarized parallel to the disk. (a) View from the top. (b) View from the side. Parameters used in the simulation: disk radius $r = 50$ nm, Fermi level $E_F = 0.5$ eV, and mobility $\mu = 10000$ cm^2/Vs	27
2-4	Universal maximum absorption of thin films between two dielectric materials with electric permittivities ϵ_1 and ϵ_2 . The maximum absorption dependence on the angle of incidence and the dielectric contrast ϵ_1/ϵ_2 is shown for s - and p - polarizations. From [55].	31

2-5	Optical absorption spectrum of a single doped graphene sheet patterned into periodic nanodisk arrays. Light is incident in the direction perpendicular to the plane of the disks, and is linearly polarized in the direction parallel to the plane of the disks. Parameters used in the simulation: disk radius $r = 30$ nm, lattice spacing $a = 78$ nm, Fermi level $E_F = 0.4$ eV, and mobility $\mu = 10000$ cm ² /Vs.	33
2-6	Optical absorption spectrum of a single doped graphene sheet patterned into periodic nanohole arrays. The absorbed power is normalized to the incident light power. Light is incident in the direction perpendicular to the plane of the disks, and is linearly polarized in the direction parallel to the plane of the disks. Parameters used in the simulation: disk radius $r = 30$ nm, lattice spacing $a = 78$ nm, Fermi level $E_F = 0.4$ eV, and mobility $\mu = 10000$ cm ² /Vs.	34
2-7	Optical absorption spectrum of doped graphene sheets patterned into periodic nanohole arrays with a fixed radius of $r = 50$ nm and a range of lattice constants ranging from 160 nm to 220 nm. The absorbed power is normalized to the incident light power. Light is incident in the direction perpendicular to the plane of the disks, and is linearly polarized in the direction parallel to the plane of the disks. Parameters used in the simulation: Fermi level $E_F = 0.7$ eV, and mobility $\mu = 10000$ cm ² /Vs.	35
2-8	Optical absorption spectrum of doped graphene sheets patterned into periodic nanohole arrays. The Fermi level of the graphene sheet is varied from 0.4 eV to 0.8 eV. The absorbed power is normalized to the incident light power. Light is incident in the direction perpendicular to the plane of the disks, and is linearly polarized in the direction parallel to the plane of the disks. Parameters used in the simulation: radius $r = 50$ nm, lattice constant $a = 180$ nm, and mobility $\mu = 10000$ cm ² /Vs.	36

2-9	A single doped graphene sheet whose conductivity is periodically spatially modulated on a nanometer scale. Inside the shaded circles, the graphene is doped at certain Fermi level that attributes the graphene regions with an optical conductivity σ_1 ; outside the shaded circles, the graphene is doped at another Fermi level hence attains a different optical conductivity σ_2	37
2-10	Analytical and numerical results for polarizability α of a conductivity modulated graphene disk as a function of frequency. Blue curves are the real parts of α ; red curves are the imaginary parts of α . Inset: Electric field around a conductivity modulated graphene disk with radius $r = 3$ nm, in the direction perpendicular to the graphene plane. The excitation electric field is linearly polarized parallel to the graphene plane, at a frequency of $f = 62.7$ THz. From [27].	38
3-1	Parallel-plate-capacitor models of (a) traditional dielectric (SiO_2 , HfO_2 , and Al_2O_3) gates, and (b) electrolyte gates. The charges at the interfaces between the sample and the dielectric (electrolyte) schematically represents the Debye screening layer.	43
3-2	Schematic representation of a graphene device double gated with the proposed electrolyte-PMMA-screen geometry. Large-area graphene (black) covers a doped Si substrate (dark gray) with a layer of HfO_2 or SiO_2 (light gray) grown on top. Above the graphene, a layer of crosslinked-PMMA (Poly(methyl methacrylate)) (purple) is defined with nanoscale structures. This PMMA layer serves as a screening layer for the solid polymer electrolyte gate (light blue) covering the entire sample. Metal (typically Au) (yellow) structures are defined to act as grounding (contacting) and gating electrodes.	44

3-3	Optical (left) and scanning-electron-microscopy (SEM) (right) images of exposed and developed negative-tone cross-linked PMMA nanostructures on Si substrate, fabricated with Raith 150 system at MIT at 30 keV using 200-nm-thick PMMA. The overexposed PMMA circles has a radius of 100 nm, and a lattice constant of 400 nm. Yellow dots: overexposed PMMA circles; blue: PMMA exposed at a normal dose due to electron diffusion; green: unexposed PMMA.	46
3-4	Chemical composition of the polymer (ethylene)oxide (PEO) and the salt lithium perchlorate (LiClO_4) (left). Upon dissolving LiClO_4 in the solvent PEO, LiClO_4 is separated into charged ions Li^+ and ClO_4^- . The highly reactive Li^+ is wrapped in PEO chains, thus protected from chemical reactions with the environment. From [15].	47
3-5	Experimental scheme and the result for testing the impenetrability of PMMA screens for charged ions from electrolyte gates. The tested Au electrode is partially covered by a PMMA screen square. Voltage is applied to a global electrolyte gate covering both areas. After a high voltage ($V > V_{break-down}$ is applied) is applied, exposed area of the electrode suffer from severe corrosion whereas protected area of the electrode remain intact.	48
3-6	Electrical measurement of a graphene $p-n$ junction. (a) Optical image of an example of fabricated large-scale CVD graphene devices. (b) Optical image of a graphene FET device consisting of contacting and gating electrodes, with a electrolyte-PMMA-screen local gate on top. Half of the graphene channel is covered by the PMMA screen. Electrolyte is not shown in this picture. (c) Resistance of the device as a function of applied electrolyte gate voltage V_{eg} under ambient conditions.	50

3-7	Optoelectronic measurements of a series of graphene p - n junctions. (a) Optical image of a graphene FET device consisting of contacting and gating electrodes, with a series of electrolyte-PMMA-screen local gates on top. The graphene channel is covered by a series of PMMA strips that are 5 μm in width. Electrolyte is not shown in this picture. (b) Photocurrent generated in the device as a function of applied electrolyte gate voltage V_{eg} under ambient conditions. Two spatial locations are measured: blue: a p - n junction formed in the middle of the graphene channel; red: the interface between graphene and the metal contact. The locations are indicated with colored dots in (a). (c) Photocurrent spatial mapping and the reflectance mapping of the graphene channel, aligned with the optical image of of the device. Colors in the photocurrent mapping denotes photocurrent direction and magnitude; colors in the reflectance mapping denotes reflected power. A laser at wavelength $\lambda = 1550$ nm with a spot size of ~ 3 μm , modulated at 100 Hz, is used to excite the photocurrent.	52
3-8	Illustration of fabrication technique for CVD graphene devices with electrolyte-PMMA-screen gates. Color: dark gray: Si substrate; light gray: back gate dielectric; thick black line: graphene; purple: PMMA; gold: Au; light blue: electrolyte; gray line: wire bonds.	54
3-9	Examples of graphene devices with electrolyte-PMMA-screen gates fabricated using procedures illustrated in Section 3.4.1.	56
4-1	Coupling between free-space (or wave-guided) mode and graphene plasmonic mode. The coupled mode theory picture of the scheme along with two cavity geometries under consideration are presented. Picture of the nanobeam cavity is from [47]; picture of the bull's eye cavity is from [51].	58

Chapter 1

Introduction

Ever since its discovery, graphene has received tremendous attention from the condensed matter physics and engineering community, both for its value in exploring fundamental physics such as properties of its massless Dirac fermions and quantum Hall effect [46, 66], and for its prospects in a variety of applications including light-harvesting in energy applications [41], transparent electrodes in electronic applications [58], photodetection and modulation in optical communication applications [23, 22], molecular detection in sensing applications[49], to name just a few. All these come from its exceptional electrical, optical, mechanical, and thermal properties.

In optics, graphene has been recognized as a promising candidate for optoelectronic and photonic applications [6] due to its strong light-matter interaction, high optical nonlinearity, and the tunability of its Fermi level by electrical gating or chemical doping. Recently, graphene plasmonics emerged as a subfield of traditional plasmonics that addresses collective charge oscillations in metallic surfaces. Compared to noble metals, plasmons in graphene have the additional benefits of longer collective oscillation lifetimes and electrical tunability [25]. In addition, its plasmonic resonances reside in the infrared to terahertz frequency range (typically from 10 to 4000 cm^{-1}), which is finding a wide variety of applications such as imaging, spectroscopy, medical sciences, communications, and information processing.

This thesis is concerned with the infrared plasmonics in graphene, in particu-

lar in graphene nanostructures. Simulations and theoretical predictions of localized plasmons in graphene nanostructures of different geometries are presented with an implication of their strongly enhanced optical absorption. The simulations then guide the experimental approach to realize infrared plasmonics in graphene nanostructures. A novel geometry of creating nanoscale carrier density modulation in graphene is proposed. Such technique can be applied to a variety of device designs of graphene and even other 2D materials, showing great prospects for numerous electronic and optoelectronic applications.

In Chapter 1, we first provide a quick overview of graphene's properties, with a focus on graphene's absorption characteristics and its optical conductivity. We then start introducing graphene surface-plasmon-polaritons (SPP), the topic of this thesis. We provide a theoretical background on the calculation of graphene's plasmonic mode dispersion, together with experimental approaches for its characterization.

In Chapter 2, we deal with localized plasmons in graphene nanostructures. Simulations and theoretical calculations of plasmonic modes in graphene nanostructures and their periodic arrays are investigated, with an implication of their application in enhancing the optical absorption of graphene films.

In Chapter 3, we discuss the experimental approach to realize the graphene nanostructures demonstrated in Chapter 2. A novel geometry is proposed and proof-of-principle testings of the geometry are conducted. Finally fabrication procedures for this technique is illustrated and various devices realized with this technique are presented.

In the last Chapter, we give an outlook for future studies that will be pursued following this thesis.

1.1 Overview of graphene properties

Graphene has a 2D honeycomb lattice structure with one atom thin thickness. The typical value for the thickness used in the literature in the calculation of optical properties is $d_g \simeq 3.3 \text{ \AA}$ [28]. In the reciprocal momentum space, the lattice structure

is honeycomb as well, as shown in Fig. 1-1. The band structure near the lattice symmetry points K and K' are linear in all directions with the same slope, forming a conical shape which is called Dirac cone:

$$E_{\pm}(\vec{k}) = \pm v_F |\vec{k}| \quad (1.1)$$

where \vec{k} is the Bloch momentum, $v_F \simeq 10^6$ m/s is the Fermi velocity, and the plus and minus signs denote the electron band and the hole band, respectively.

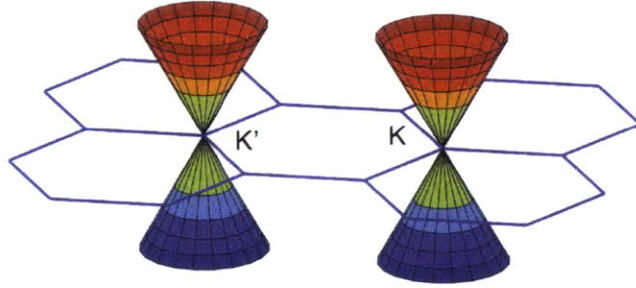


Figure 1-1: Graphene's lattice structure in momentum-space and graphene's electronic band structure (Dirac cones) at K and K' points. From [1].

Because of this unique band structure, graphene has a semi-metal nature (since there is no energy gap) and its optical conductivity is frequency-independent in a broad range of photon energies, meaning that the absorption remains a constant ($\pi\alpha = 2.3\%$ [40]) in a broad frequency range. At low photon energy levels (infrared and terahertz), the optical conductivity (and absorption) depends on the Fermi level E_F (also called the chemical potential μ) of graphene. These absorption characteristics are illustrated in Figure 1-2.

The optical conductivity of graphene has been theoretically derived from the Kubo formula within Random Phase Approximation (RPA) [3, 17]. Below we provide a summary of the result. The optical conductivity σ of graphene can be expressed in a form consisting of intraband and interband contributions:

$$\sigma = \sigma_{intra} + \sigma'_{inter} + i\sigma''_{intra} \quad (1.2)$$

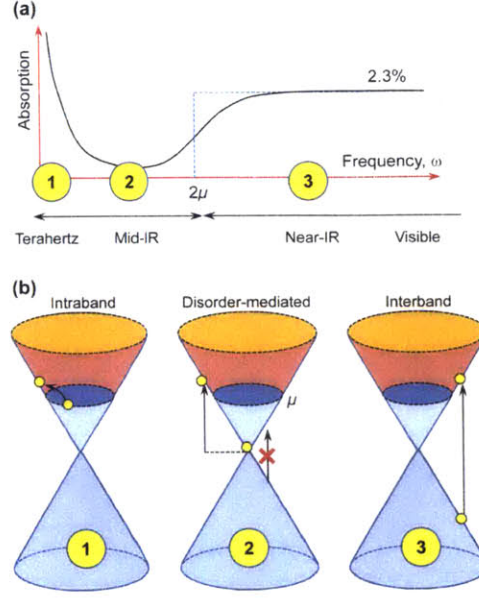


Figure 1-2: Characteristics of optical absorption in graphene. (a) A typical absorption spectrum of graphene. (b) Illustration of various optical transition processes. From [39].

The intraband contribution dominates in the infrared and terahertz range when the graphene is doped and $\mu > \hbar\omega/2$:

$$\sigma_{intra} = \frac{ie^2\mu}{\pi\hbar^2(\omega + i\tau_1^{-1})} \quad (1.3)$$

where τ_1 is the carrier relaxation time for intraband transitions, e is the elementary charge, \hbar is the reduced Plank constant and ω is the light frequency. This is the frequency range where graphene's surface-plasmon-polariton (SPP) is supported.

For slightly doped graphene ($\mu < \hbar\omega/2$), the interband transition dominates for a wide bandwidth from visible to near-infrared:

$$\sigma'_{inter} = \frac{e^2}{4\hbar} \left(1 + \frac{1}{\pi} \arctan \frac{\hbar\omega - 2\mu}{\hbar\tau_2^{-1}} - \frac{1}{\pi} \arctan \frac{\hbar\omega + 2\mu}{\hbar\tau_2^{-1}} \right) \quad (1.4)$$

$$\sigma''_{inter} = -\frac{e^2}{4\hbar} \frac{1}{2\pi} \ln \frac{(\hbar\omega + 2\mu)^2 + \hbar^2\tau_2^{-2}}{(\hbar\omega - 2\mu)^2 + \hbar^2\tau_2^{-2}} \quad (1.5)$$

where τ_2 is the carrier relaxation time for interband transitions.

At zero temperature, the total optical conductivity can be written as [17]

$$\begin{aligned}
\sigma &= \sigma_{intra} + \sigma_{inter} \\
&= \frac{ie^2\mu}{\pi\hbar^2\omega} + \frac{e^2}{4\hbar} \left[\theta(\hbar\omega - 2\mu) - \frac{i}{2\pi} \ln \frac{(\hbar\omega + 2\mu)^2}{(\hbar\omega - 2\mu)^2} \right] \\
&= \frac{ie^2}{4\hbar\pi} \left[\frac{4\mu}{\hbar\omega} - \frac{1}{2} \ln \frac{(\hbar\omega + 2\mu)^2}{(\hbar\omega - 2\mu)^2} - i\pi\theta\left(\frac{\hbar\omega}{2\mu} - 1\right) \right]
\end{aligned} \tag{1.6}$$

Both interband and intraband transitions depends on the Fermi level (chemical potential) of graphene, which in turn is related to its carrier density n by $\mu = \hbar v_F \sqrt{\pi n}$ [36]. Therefore, the optical conductivity of graphene can be altered with the carrier density. Because of graphene's 2D nature, its carrier density can be changed by electrical gating or chemical doping method. Hence the tunability of graphene's optical conductivity opens an avenue for utilizing graphene as a medium in various photonic and optoelectronic fields.

1.2 Graphene surface-plasmon-polaritons (SPP)

Traditional plasmonics emerged from plasmons confined to the surface of metals, as the prerequisite for plasmonic oscillation is that $\epsilon_r \epsilon_m(\omega) < 0$, which requires the electric permittivity of the material to be negative. This condition is normally satisfied in noble metals such as silver and gold. As a semi-metal, graphene's electric permittivity can also fall in this regime in the infrared and terahertz region. As localized plasmons typically have wavelengths much smaller than wavelength of light in air at the same frequency, they provide a confinement of light that enables control of optical field down to the nanometer scale. It is this light concentration that offers plasmonics its greatest promise in photonics. Although progress utilizing this light confinement such as surface-enhanced Raman spectroscopy [43], interface with quantum emitters [7], and enhanced absorption in photodetectors [63] has been made, a search for better plasmonic materials with greater confinement and better control of the electromagnetic field and lower losses is still underway [59]. Graphene, with its

extremely high carrier mobility and tunable Fermi level, has emerged as a promising new plasmonic material. Its extreme light confinement (a Purcell enhancement of $10^6 - 10^7$ [34]), tunability of its plasmonic modes, and the resonance wavelengths in the infrared and terahertz region guarantee an expansion of the existing plasmonic technologies to infrared and terahertz wavelengths and improvements of performance compared to existing materials.

1.2.1 Graphene plasmonic mode dispersion

To understand graphene's great potential in the field of plasmonics, it is important to look at graphene's plasmonic mode dispersion. Here we follow the derivation in [39] to provide a summary of the derivation of graphene's plasmonic dispersion.

By solving Maxwell's equation with appropriate boundary conditions, graphene's SPP mode dispersion can be written as

$$q \simeq \frac{i2\omega\epsilon_r\epsilon_0}{\sigma(q, \omega)} \quad (1.7)$$

In the long wavelength ($q \ll k_F$) and high doping ($\hbar\omega \ll E_F$) limit, graphene's optical conductivity is dominated by intraband contribution from the Drude model. Inserting Equation 1.2 into the above equation leads to

$$q(\omega) = \frac{\epsilon_r}{2\alpha} \frac{\omega}{\omega_F} k_0 \left(1 + \frac{i}{\tau\omega}\right) \quad (1.8)$$

Setting $\tau_e = 0$ gives us

$$\omega_{\text{pl}} = \sqrt{\frac{e^2 E_F q}{2\pi \hbar^2 \epsilon_r \epsilon_0}} \quad (1.9)$$

We note that this plasmon dispersion relation has a square root dependence, which is expected for all 2D systems [54].

When photon energy increases or the Fermi level of graphene decreases, the long wavelength and high doping limit breaks down. In this regime, the plasmon dispersion can be calculated by considering zeros of graphene's electric permittivity within Random Phase Approximation (RPA). The mathematical details for this calculation

can be found in [30, 60]. The full calculated graphene plasmon dispersion is shown in Figure 1-3(a). We note that at low photon energies, the plasmon dispersion in the

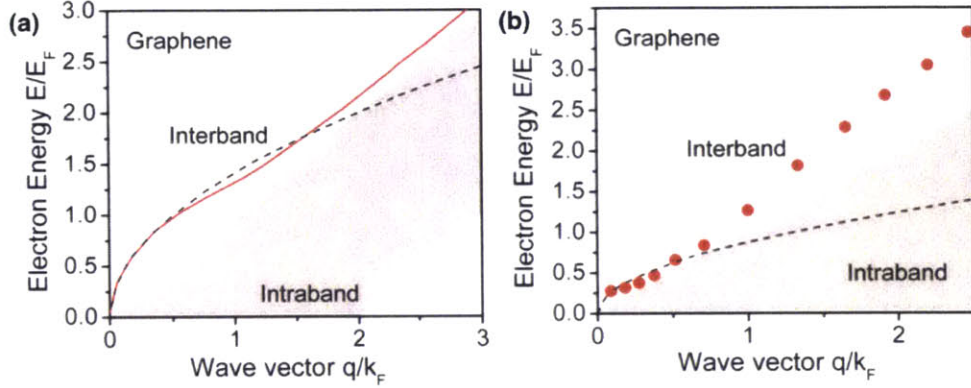


Figure 1-3: (a) Plasmon dispersion of graphene calculated within Random Phase Approximation. Black dash line indicates plasmon dispersion in the long wavelength and high doping limit. Gray shades indicate regions where Landau damping from electron-hole pair excitations becomes prominent. From [30]. (b) Plasmon dispersion of graphene measured using Electron Energy Loss Spectroscopy (EELS) with graphene on SiC. From [38].

long wavelength and high doping limit (black dash line) is in good agreement with the full theoretical calculation. The gray shaded areas denote Landau damping regions where plasmons become severely damped with intraband and interband electron-hole pair excitations and can no longer be sustained.

Figure 1-3(b) shows the plasmon dispersion of graphene experimentally measured with the Electron Energy Loss (EELS) technique, where a graphene sample on SiC substrate is exposed to an electron beam and the energy loss of the reflected and transmitted beam is measured and analyzed to infer the plasmon dispersion [39].

Chapter 2

Enhanced optical absorption with confined graphene plasmons in nanostructures

So far our discussion has been focused on surface plasmons in extended graphene sheets; however, inducing graphene plasmons in nanometer-sized structures yields additional benefits such as extreme optical field confinement, enhanced light-graphene interaction, and an additional degree of freedom for plasmonic resonance tuning by engineering the size and shape of nanostructures. In this thesis, we are mainly concerned with localized infrared graphene plasmons generated in nanodisks. In particular, we will consider enhanced light absorption as a manifestation of graphene plasmons, as it plays an important role in various applications such as graphene photodetection and nonlinear optics.

How light interacts with particles whose size is much smaller than the light wavelength has long been studied [42]. Such a problem can be solved by applying Maxwell's equations with the same bulk material dielectric properties, but with modified boundary conditions arising from reduced size of the nanoparticles. When certain conditions are met, discontinuities in electric permittivity give rise to localized plasmon oscillations confined to the surface of the conductors [37]. Similarly, graphene ribbons [44], disks [56] and their periodic arrays [45, 55] can also support localized plas-

monic modes, and initial evidences of such plasmonic modes have been experimentally observed in a number of patterned graphene micro/nanostructures [18, 33, 61, 62]. Figure 2-1 shows two examples of experimental observation of graphene plasmons in

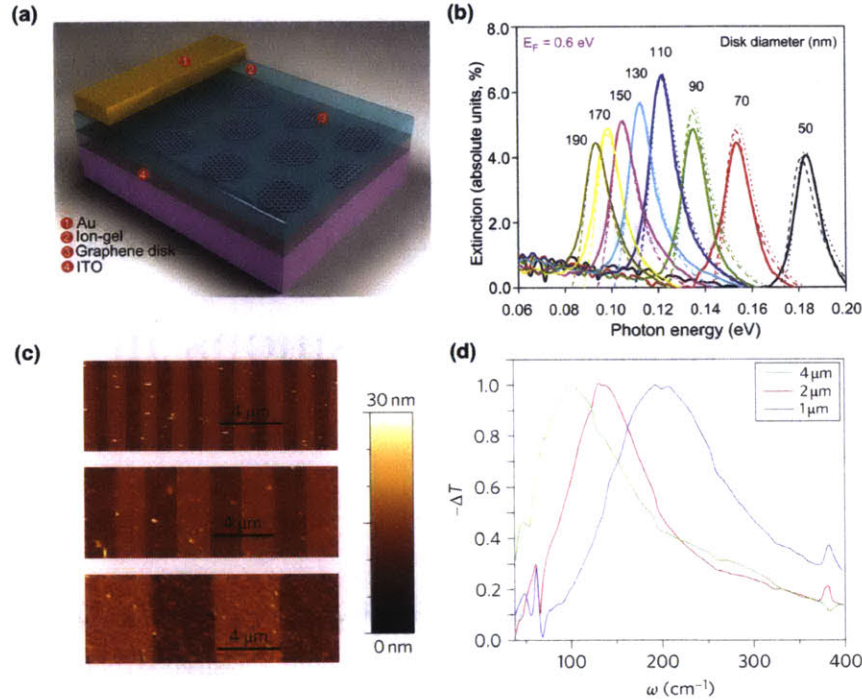


Figure 2-1: Experimental observation of graphene surface plasmons in patterned graphene micro/nanostructures. (a) Schematic diagram of patterned graphene nanodisk arrays on top of an ITO-coated silica substrate. (b) Experimental and theoretical extinction spectra for fixed doping of graphene nanodisks ($E_F = 0.61$ eV) and varying disk diameter (50 - 190 nm). The extinction is given in difference percentage between regions with and without graphene. (c) AFM images of patterned graphene microribbons with varying width (1 - 4 μm). (d) Change of transmission spectra with different graphene microribbon widths for the same doping concentration of $1.5 \times 10^{13} \text{cm}^{-2}$. All spectra were normalized by their respective peak values for convenience of comparison. (a)(b) from [18]; (c)(d) from [33].

patterned graphene micro/nanostructures, and how plasmonic resonances shift with varying structure dimensions. Figure. 2-1(a)(b) shows plasmonic resonances observed in patterned graphene nanodisk arrays; Figure. 2-1(c)(d) shows plasmonic resonances observed in patterned graphene microribbons. Both structures have been tested with far-field infrared/terahertz transmission/absorption spectroscopy measurements.

Compared to nanoribbons, nanodisks have the benefits of providing plasmon con-

finements in all directions, enabling plasmonic resonances at a higher photon energies compared to nanoribbons and giving rise to narrower resonances [34]. In this chapter, we provide the theoretical framework and numerical simulations for understanding localized plasmons in graphene nanodisks, nanodisk/nanohole arrays, and nanoscale conductivity modulation structures. First, graphene nanodisks and their plasmonic modes are introduced, including their extreme light confinement ability and its implication in light-graphene interaction. After that we consider plasmonic modes in periodic graphene nanostructures and its manifestation in increased optical absorption of graphene films with nanostructures. Different geometries (nanodisk, nanohole, nanoscale conductivity modulation arrays) are demonstrated, and the effects of varying parameters such as nanostructure dimensions and Fermi level are investigated and discussed.

2.1 Plasmons in graphene nanodisks

Graphene nanodisks are nanostructured graphene sheets with a specific radius, typically on the order of tens of nanometers. It has been predicted that such nanodisks support confined, long-lived plasmons, which produce sharp IR resonances [34].

Figure 2-2 shows an example of the extinction cross section spectrum of a graphene nanodisk simulated using boundary-element method (BEM) [48], with an open-source software package SCUFF-EM [2]. The permittivity of graphene used in the simulation is obtained using local random phase approximation (local-RPA) with the analytical expressions summarized in Section 1.1. The characteristic parameters of graphene, including Fermi level and carrier mobility, are specified. In this case, the Fermi level of the graphene disk is $E_F = 0.5$ eV, and the carrier mobility is $\mu = 10000$ cm²/Vs. The radius of the disk is $r = 50$ nm. The incident light is a plane wave in the direction perpendicular to the plane of the disk, and is linearly polarized in the direction parallel to the disk. The extinction cross section spectrum is well described by a Lorentzian line shape, with a prominent resonance when the incident free space light has a wavelength of roughly 7 μ m. The resonance corresponds to

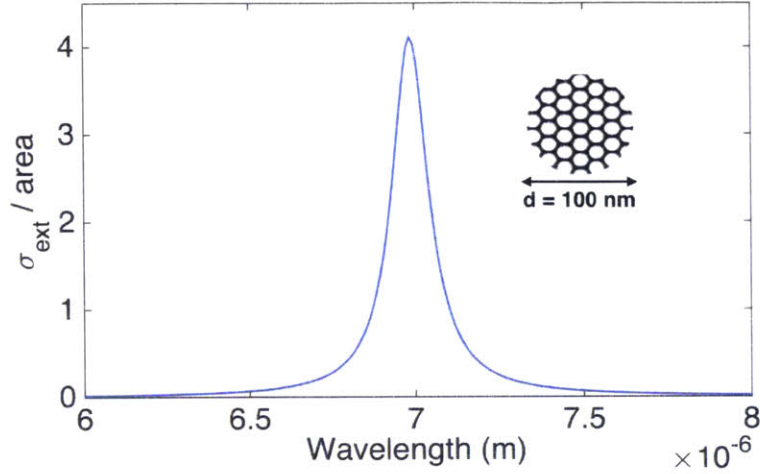


Figure 2-2: Extinction cross section of a doped graphene nanodisk normalized to the geometrical area of the disk, showing a prominent resonance characteristic of a dipolar plasmon excited in the nanodisk. Parameters used in the simulation: disk radius $r = 50$ nm, Fermi level $E_F = 0.5$ eV, and mobility $\mu = 10000$ cm²/Vs.

a localized plasmonic mode of the disk, at which the extinction cross section can exceed 4 times the geometrical area of the disk itself, interestingly. At higher Fermi levels, the extinction cross section can exceed the physical area by over an order of magnitude [55], which is comparable to atoms when the incoming field is at resonance.

In general, the optical response of graphene nanostructures can be described by the polarizability [31, 18]

$$\alpha(\omega) = D^3 \frac{G}{\frac{2K}{\epsilon_1 + \epsilon_2} - \frac{4\pi\epsilon_0 i \omega D}{\sigma(\omega)}} \quad (2.1)$$

where ω is the frequency of the incident light, ϵ_1 and ϵ_2 are the electric permittivities of the dielectrics defining the interface where the nanostructure is sitting, and σ is the optical conductivity of graphene. D is a parameter that is dependent on the dimension of the nanostructure; in the case of a nanodisk, it represents the diameter of the disk. The constants G and K are independent of the frequency of the incident light, the dielectric environment, and the structure dimension, but are characteristic of the symmetry of the excited plasmon. For the lowest-order dipolar disk plasmon, $G = 0.65$ and $K = 12.5$ [18]. With the polarizability of a graphene nanodisk $\alpha(\omega)$,

the extinction cross section can then be calculated using $\sigma_{\text{ext}} = (4\pi\omega/c)\text{Im}\{\alpha(\omega)\}$ ¹.

Figure 2-3 shows the scattered electric field intensity around the graphene nanodisk corresponding to the plasmonic mode at 7 μm illustrated in Figure 2-2, normalized to the field intensity without graphene. From the side view of the disk(Figure 2-

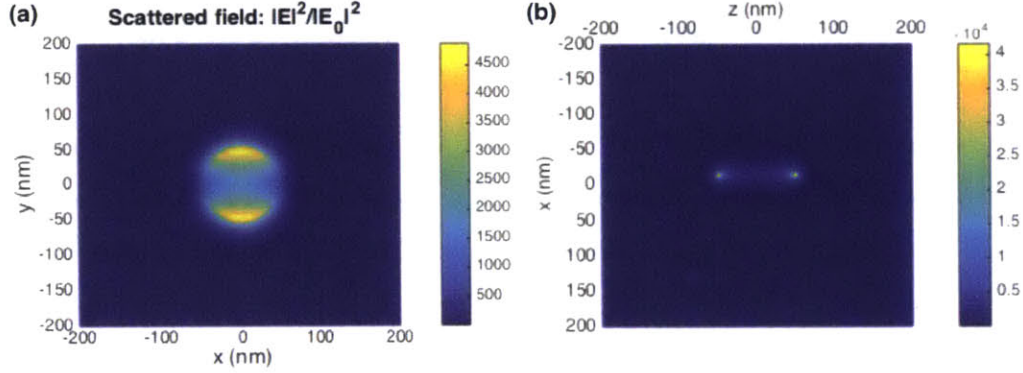


Figure 2-3: Scattered electric field intensity around a graphene nanodisk corresponding to a graphene plasmonic disk mode at 7 μm , normalized to the field intensity without any graphene. Light is incident perpendicular to the disk plane (xy-plane), linearly polarized parallel to the disk. (a) View from the top. (b) View from the side. Parameters used in the simulation: disk radius $r = 50$ nm, Fermi level $E_F = 0.5$ eV, and mobility $\mu = 10000$ cm^2/Vs .

2(b)), it can be seen that the field is strongly confined to the surface of the disk, and its intensity can be enhanced by as high as four orders of magnitude on the edge of the disk. This extreme light confinement and enhancement is essential to many applications that require strong interaction between light and materials. Below, we illustrate an implication of this strong field enhancement in the context of nonlinear optics.

An intuitive picture of nonlinearities associated with electrons(atoms) in materials is that the electric field induced by an incident light in the material is strong enough to alter the intrinsic electric field maintained by the electrons(atoms) of the material, such that the original material properties are modified. Therefore we can gain some insight from calculating the existing electric field amplitude of graphene and compare it with the electric field amplitude when a plasmonic mode is excited inside a graphene

¹Extinction cross section is the sum of absorption cross section and scattering cross section: $\sigma_{\text{ext}} = \sigma_{\text{abs}} + \sigma_{\text{scat}}$.

nanodisk [31].

Typically, graphene is doped to a carrier density of $n = 10^{12} \text{ cm}^{-2} - 10^{13} \text{ cm}^{-2}$, which correspond to a distance between electrons(or holes) of $r_e = 1/\sqrt{n\pi} \simeq 5 \text{ nm}$. Hence, the intrinsic electric field is roughly [31]

$$E_e = \frac{e}{4\pi\epsilon_r\epsilon_0r_e^2} \simeq 2 \times 10^7 \text{ V/m.} \quad (2.2)$$

We have simulated the electric field amplitude induced by a plasmonic mode inside a graphene nanodisk, as shown in Figure 2-3. At a field intensity enhancement of about 10^4 , the field amplitude is enhanced by a factor of about 10^2 . As the incident electric field amplitude is $1 \times 10^6 \text{ V/m}$, the induced electric field by the graphene plasmonic disk mode can reach a field amplitude up to about 10^8 V/m , which is about the same order of magnitude as the intrinsic electric field in graphene. At this field strength, an external field can no longer drive a self-sustained charge density oscillation; in other words, if there exists a single plasmon quantum in a graphene nanodisk, no plasmons can be further excited in the same disk. This is the **plasmon blockade effect**; it plays an important role in applications such as all-optical switches in optical communications. A rigorous derivation of the multi-plasmon damping rates can be found in [31].

2.2 Enhanced optical absorption with periodic nanostructures in graphene

Optical absorption is essential for various promising prospects of graphene optical applications, including light harvesting, optical detection, spectral photometry and optical modulation. Although absorption of suspended graphene in air, 2.3%, is exceptional for a single atomic layer of material, its absolute absorption is relatively small. Recent effort has been seen on pursuing a way of increasing the optical absorption of graphene, including integrating graphene with optical waveguides on chip [23], photonic-crystal-cavity resonators [22], and metal plasmonic antenna struc-

tures [35, 19]. Due to graphene plasmon's extreme light confinement and field enhancement ability, graphene plasmonic nanostructure has also been proposed as a candidate for boosting optical absorption in graphene, and it has indeed been predicted that complete optical absorption can be achieved in periodic arrays of graphene nanoresonators, under the condition that the absorption cross section of each nanoresonator is comparable to the area of a unit cell in the array [55, 24].

Progress towards experimental implementations of this concept has been made [18, 20, 32], making use of nanodisk and nanoribbon geometries. However, optical absorption of only $\sim 30\%$ has been reported so far. Two main reasons underlie the experimental failure of attempts to realize the theoretically predicted perfect absorption: (1) In simulations, the doping level of graphene sheets can be trivially specified by assigning them the corresponding optical conductivity and electrical permittivity. However, it is experimentally tricky to dope graphene to an arbitrarily high Fermi level (a Fermi level of ~ 0.5 eV is typically attainable with a dielectric (SiO_2 , HfO_2) gate [62], ~ 1 eV is attainable with an electrolyte gate [16]), and nanodisk/nanoribbon geometries provide further difficulties for effective doping, as an additional structure (such as ITO) must be included to provide the same electrical ground potential for the numerous disks. (2) While the use of nanostructures provide a convenient way of accessing the plasmonic excitations, edge scatterings that are not considered in simulations result in higher damping rates of the plasmonic modes, reducing the optical absorption of the patterned graphene sheets.

To deal with the first obstacle, a stable and effective gating method of graphene nanostructures is desirable. To this end, we propose two new geometries utilizing the concept proposed in [55], periodic nanohole(antidisk) arrays in patterned graphene and periodic nanoscale conductivity modulation in extended graphene, whose connected structure solves the problem of ineffective doping of discrete nanodisks. In particular, our proposed periodic nanoscale conductivity modulation method in extended graphene, whose experimental implementation will be discussed in details in Chapter 3, additionally solves the second problem. Combined with our experience in handling of the electrolyte gate, the new geometries have higher potential in realizing

the predicted perfect absorption in a controllable and reliable way.

In this section, theoretical and simulation results of enhanced optical absorption with nanostructures in graphene are presented and discussed. To begin with, we first provide an overview of general optical absorption in thin films, including the fundamental limits of absorption in thin films under different configurations. We then consider periodic nanodisk arrays as a proof-of-principle study. After this, we investigate the absorption properties of our proposed nanohole and nanoscale conductivity modulation geometries by providing a simulation and theoretical study of the nanostructures and their arrays.

2.2.1 Universal limit to absorption in thin films - an overview

Consider a thin film in a symmetric environment, where the electric permittivities ϵ_1 and ϵ_2 of the dielectric materials on both sides of the thin film are the same. The absorption of the thin film can be written as [55]

$$A = 1 - |r|^2 - |1 \pm r|^2 \quad (2.3)$$

where r is the reflection coefficient of the thin film, and the “+” (“-”) sign is for s - (p -) polarized light. When $r = \pm 1/2$, A reaches a maximum value of 50%. When an asymmetric environment is considered ($\epsilon_1 \neq \epsilon_2$), the absorption of the thin film can be increased, and can reach 100% maximum absorption under certain conditions. This universal maximum absorption of thin films is studied in [55], and analytical expressions for them are derived [55]

$$A_{s,\max} = \frac{1}{1 + \text{Re}\{f\}} \quad (2.4)$$

$$A_{p,\max} = 1 - \frac{\text{Re}\{f\}}{\text{Re}\{f\} + (\epsilon_1/\epsilon_2)|f|^2} \quad (2.5)$$

where $f = (\epsilon_2/\epsilon_1 - \sin^2 \theta)^{1/2} / \cos \theta$, and θ is the angle of incidence. The dependence of this universal maximum absorption on the angle of incidence and ϵ_1/ϵ_2 is shown

in Figure 2-4. This 2D-contour provides us with a guide on the fundamental limits

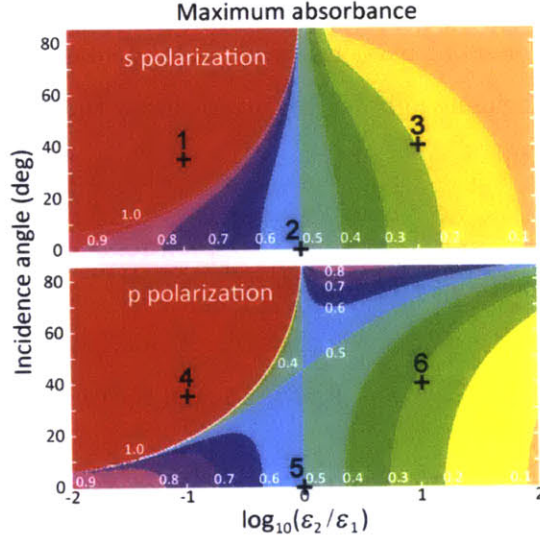


Figure 2-4: Universal maximum absorption of thin films between two dielectric materials with electric permittivities ϵ_1 and ϵ_2 . The maximum absorption dependence on the angle of incidence and the dielectric contrast ϵ_1/ϵ_2 is shown for *s*- and *p*-polarizations. From [55].

of thin film absorption, and an idea of the room of improvement for our simulated structures in terms of optical absorption.

2.2.2 Periodic nanodisk arrays in patterned graphene

Before we start the discussion of specific geometries, we note that all nanostructures and their arrays simulated in this thesis are free-standing in air, meaning that the thin films under consideration are located in a symmetric environment. Hence, the maximum optical absorption that can be achieved in our simulation is 50%. Graphene nanostructures in asymmetric environments are not simulated for this thesis, but they should in principle show similar characteristic behaviors, in terms of the dependence of optical absorption on dimension, spacing and Fermi level of the graphene nanostructures. Under certain dielectric contrast conditions, we should also expect higher optical absorption due to total internal reflection (TIR) and suppressed reflection arising from the asymmetric environments.

We first consider a periodic array of graphene nanodisks, which has been studied by Thongrattanasiri *et al.* [55], as a pedagogical example. In general, for a thin film consisting of an array of small particles, whose lattice constant a is small compared to the wavelength of incident light, it has been shown that its reflection coefficient can be written as [12, 55]

$$r = \frac{\pm iS}{\alpha^{-1} - G} \quad (2.6)$$

where α is the polarizability of the small particle, and S, G are lattice dependent parameters. $S = 2\pi\omega/cA \cos \theta$ ($S = 2\pi\omega \cos \theta/cA$) for s - (p -) polarized light, where A is the unit-cell area. $\text{Im}(G) = S - 2(\omega/c)^3/3$, and $\text{Re}(G) \simeq g/a^3$, with $g = 4.52$ for square lattices.

For graphene nanodisks, this reflection coefficient can be calculated by inserting the polarizability of the nanodisks into Equation 2.1. The condition for maximum absorption ($r = \pm 1/2$) dictates that $\zeta = 1/2$, where ζ is defined as [55]

$$\zeta = \frac{A}{\sigma_{\max}^{\text{ext}}} \cos \theta, \text{ } s\text{- polarization} \quad (2.7)$$

$$\zeta = \frac{A}{\sigma_{\max}^{\text{ext}}} \cos^{-1} \theta, \text{ } p\text{- polarization} \quad (2.8)$$

The resonance (maximum absorption) is obtained at $\omega \simeq \omega_p - 3gk_r/4(\omega_p a/c)^3$, which is slightly redshifted from the plasmonic resonance of a single graphene nanodisk ω_p [55]. From the maximum absorption conditions in Equations 2.7 and 2.8, it can be seen that the condition can be fulfilled at the resonant wavelength by adjusting the spacing of the nanodisks, given certain maximum extinction cross section corresponding to a graphene nanodisk.

Indeed, by fixing the nanodisk radius to be $r = 30$ nm and varying the lattice spacing a , we are able to simulate a thin film of doped graphene nanodisk arrays whose optical absorption can reach a maximum of 50% at a resonant wavelength of ~ 6.5 μm . The optical absorption spectrum of such a thin film is shown in Figure 2-5. Again, the numerical simulation is performed using the software package SCUFF-

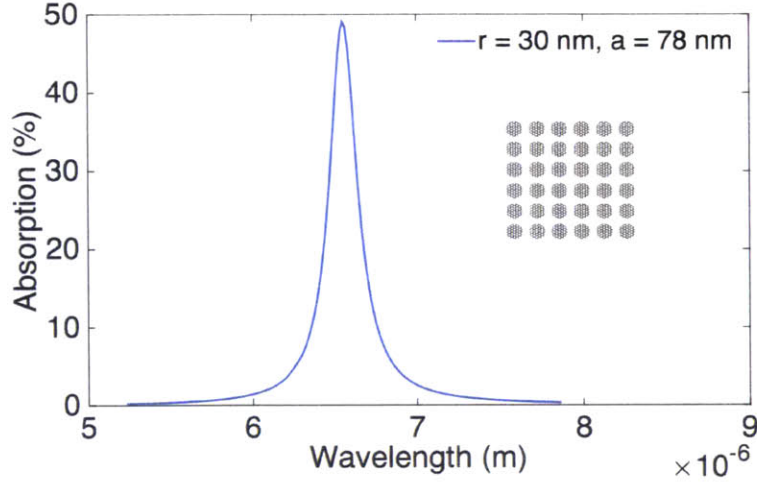


Figure 2-5: Optical absorption spectrum of a single doped graphene sheet patterned into periodic nanodisk arrays. Light is incident in the direction perpendicular to the plane of the disks, and is linearly polarized in the direction parallel to the plane of the disks. Parameters used in the simulation: disk radius $r = 30$ nm, lattice spacing $a = 78$ nm, Fermi level $E_F = 0.4$ eV, and mobility $\mu = 10000$ cm²/Vs.

EM [2]. The incident light is a plane wave in the direction perpendicular to the plane of the nanodisks, and is linearly polarized in the direction parallel to the disk. The radius of the disks is chosen to be $r = 30$ nm because it is experimentally realistic to define such disks using electron beam lithography method [5], and the resultant resonant wavelength also falls in the mid-infrared regime of our interest.

2.2.3 Periodic nanohole(antidisk) arrays in patterned graphene

As mentioned above, although patterning discrete graphene nanodisk arrays is a convenient way of exciting plasmonic modes and increasing optical absorption of the graphene film, realistically it is hard to reliably dope all the discrete disks to a certain Fermi level due to the structure's disconnectivity. To cope with this problem, we investigate the inverse structure of a periodic nanodisk array - a periodic nanohole(antidisk) array, consisting of nanoscale holes forming a square lattice that are etched from the extended graphene sheet. In terms of effective doping, this structure is more desirable because the connectivity of the graphene sheet allows charge carriers to be transported efficiently when electrical gate is applied. The structure can

be gated either with dielectrics such as SiO_2 and HfO_2 from the back using substrates coated with those materials, or with electrolyte from the top using spin-coating or dip-coating.

Figure 2-6 shows the simulated optical absorption spectrum of a doped graphene sheet patterned with periodic nanoholes with a radius of $r = 30$ nm and a lattice constant of $a = 78$ nm. Again the spectrum is simulated with the software package

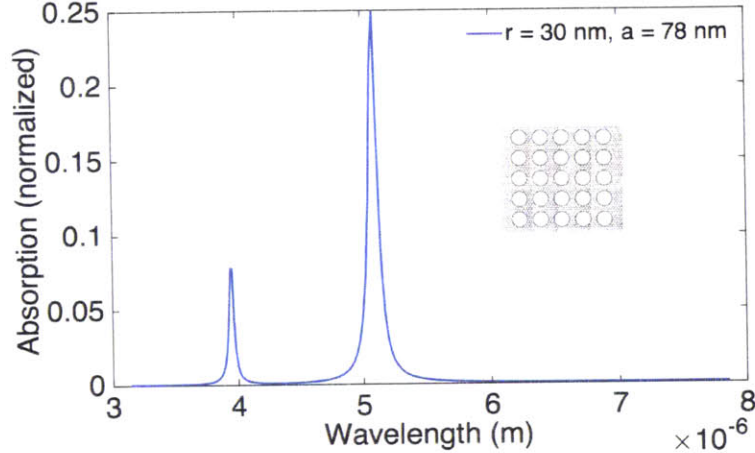


Figure 2-6: Optical absorption spectrum of a single doped graphene sheet patterned into periodic nanohole arrays. The absorbed power is normalized to the incident light power. Light is incident in the direction perpendicular to the plane of the disks, and is linearly polarized in the direction parallel to the plane of the disks. Parameters used in the simulation: disk radius $r = 30$ nm, lattice spacing $a = 78$ nm, Fermi level $E_F = 0.4$ eV, and mobility $\mu = 10000$ cm^2/Vs .

SCUFF-EM [2], with the incident light being a plane wave in the direction perpendicular to the film with a linear polarization parallel to the film. Similar to the absorption spectrum of periodic nanodisk arrays, periodic nanohole arrays also show prominent peaks in optical absorption corresponding to resonant plasmonic modes, with a fundamental mode at $\lambda \simeq 4.6$ μm and a 1st excited mode at $\lambda \simeq 3.4$ μm . Since the fundamental mode shows higher optical absorption in the film, from now on we only consider this fundamental mode. We can again vary the spacing of the holes to optimize the total absorption of the film.

Figure 2-7 shows the simulated optical absorption spectrum of doped graphene sheets patterned with periodic nanoholes with a fixed radius of $r = 50$ nm and a

range of lattice constants from 160 nm to 220 nm. When the lattice spacing is

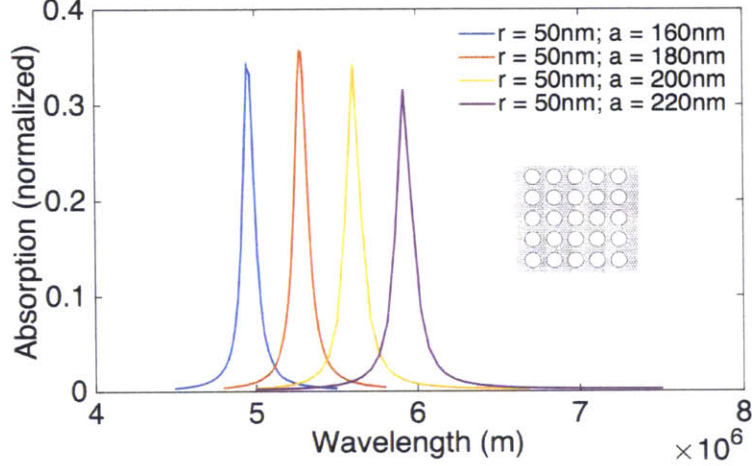


Figure 2-7: Optical absorption spectrum of doped graphene sheets patterned into periodic nanohole arrays with a fixed radius of $r = 50$ nm and a range of lattice constants ranging from 160 nm to 220 nm. The absorbed power is normalized to the incident light power. Light is incident in the direction perpendicular to the plane of the disks, and is linearly polarized in the direction parallel to the plane of the disks. Parameters used in the simulation: Fermi level $E_F = 0.7$ eV, and mobility $\mu = 10000$ cm^2/Vs .

180 nm, the maximum optical absorption reaches its optimal value. We note that although the simulated absorption is not as high as for the nanodisk arrays, the maximum absorption can be further enhanced by increasing the carrier mobility of the graphene or doping it to a higher Fermi level, as will be illustrated below.

Figure 2-8 shows the simulated optical absorption spectrum of doped graphene sheets patterned with periodic nanoholes with fixed radius of $r = 50$ nm and lattice constant of $a = 180$ nm. The Fermi level of the graphene sheet is varied from 0.4 eV to 0.8 eV. As the Fermi level of the doped graphene increases, the resonant wavelength blueshifts and the optical absorption increases. The resonant modes also show smaller FWHMs, i.e., higher quality (Q) factors.

Therefore, we can push the optical absorption to the limit of 50% by increasing the Fermi level, which further provides us with the benefits of lower damping rates of the localized plasmons and longer lifetimes. Additionally, the shifting of the resonant wavelength with the graphene Fermi level indicates a convenient way of *in situ*

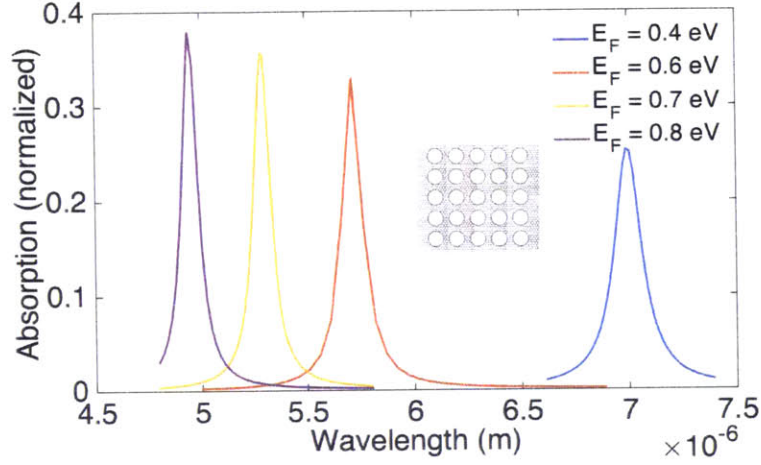


Figure 2-8: Optical absorption spectrum of doped graphene sheets patterned into periodic nanohole arrays. The Fermi level of the graphene sheet is varied from 0.4 eV to 0.8 eV. The absorbed power is normalized to the incident light power. Light is incident in the direction perpendicular to the plane of the disks, and is linearly polarized in the direction parallel to the plane of the disks. Parameters used in the simulation: radius $r = 50$ nm, lattice constant $a = 180$ nm, and mobility $\mu = 10000$ cm^2/Vs .

tuning of the central wavelength of absorption peaks without modifying the geometry. Therefore, the promising prospect of utilizing periodic graphene nanostructures in applications involving strong and tunable optical absorption relies heavily on the effective and stable control of the Fermi level of graphene nanostructures.

2.2.4 Periodic nanoscale conductivity modulation in extended graphene

The second issue that prevents experimental implementations of graphene periodic nanodisk arrays from realizing the predicted perfect optical absorption is the presence of edge scattering from patterned graphene nanostructures that is not considered in the numerical simulations. This issue again shows up in the periodic nanohole arrays geometry we present above. For this reason, alternative ways of exciting plasmonic modes in extended graphene sheets are desirable. Hence, here we propose the periodic nanoscale conductivity modulation geometry, which eliminates the drawback of edge

scattering by keeping an extended sheet of unpatterned graphene, and at the same time maintains the concept of utilizing periodic graphene nanostructures that support plasmonic modes.

The proposed periodic conductivity modulation geometry is shown in Figure 2-9. The diameter of the shaded circles is typically ~ 50 nm. Inside the shaded circles, the

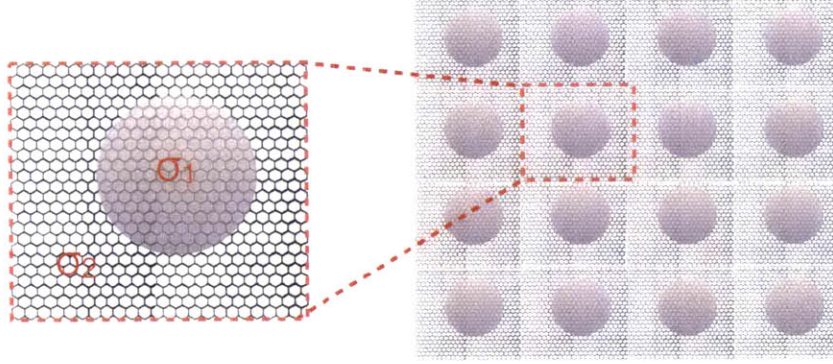


Figure 2-9: A single doped graphene sheet whose conductivity is periodically spatially modulated on a nanometer scale. Inside the shaded circles, the graphene is doped at certain Fermi level that attributes the graphene regions with an optical conductivity σ_1 ; outside the shaded circles, the graphene is doped at another Fermi level hence attains a different optical conductivity σ_2 .

graphene is doped at certain Fermi level that attributes the graphene region with an optical conductivity σ_1 ; outside the shaded circles, the graphene is doped at another Fermi level hence attains a different optical conductivity σ_2 .

Previously in the case of graphene nanodisk arrays, we started from the general expression (Equation 2.6) for the reflection coefficient of a thin film consisting of an array of small particles:

$$r = \frac{\pm iS}{\alpha^{-1} - G} \quad (2.9)$$

By inserting the polarizability of the graphene nanodisk into this expression and solve for the maximal absorption condition, we reached the conclusion that by adjusting the spacing of the nanodisks we can get the optimal 50% absorption, and the optical response is only slightly redshifted from the plasmonic response of a single graphene nanodisk.

Similarly, we can get an idea of the optical response of a periodically conductivity modulated graphene sheet by investigating the polarizability of its unit cell, as shown in Figure 2-9. It is found that the polarizability of such a conductivity modulation unit cell is described by [27]

$$\alpha = \frac{\pi R^2}{-i\omega} \left[2\sigma_1\sigma_2 + \frac{i k_0 R}{2 \eta_0} (\sigma_1 - \sigma_2) \right] \frac{1}{\sigma_1} \frac{\sigma_1 - \sigma_2}{\sigma_1 + \sigma_2}. \quad (2.10)$$

Figure 2-10 shows this polarizability plotted as a function of free-space frequency [27]. The polarizability spectrum again exhibits prominent resonant peaks at free-space frequencies of ~ 60 THz, corresponding to $\sim 5 \mu\text{m}$ in wavelengths. The electric field

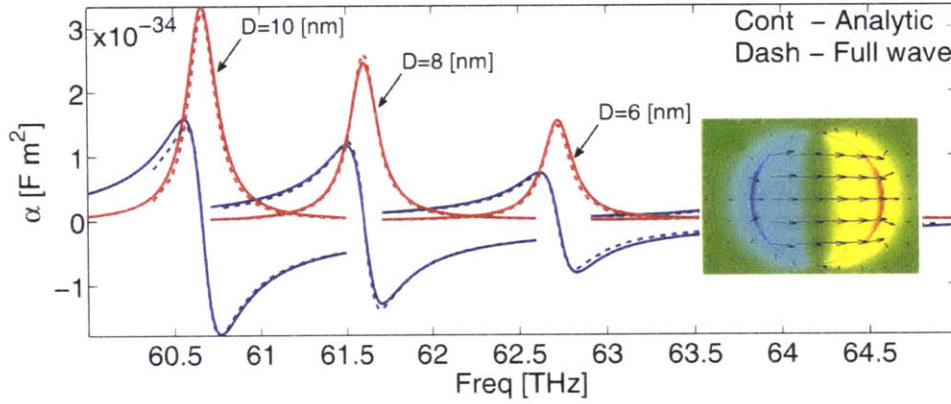


Figure 2-10: Analytical and numerical results for polarizability α of a conductivity modulated graphene disk as a function of frequency. Blue curves are the real parts of α ; red curves are the imaginary parts of α . Inset: Electric field around a conductivity modulated graphene disk with radius $r = 3 \text{ nm}$, in the direction perpendicular to the graphene plane. The excitation electric field is linearly polarized parallel to the graphene plane, at a frequency of $f = 62.7 \text{ THz}$. From [27].

around the conductivity modulated graphene disk also shows a dipolar behavior that is similar to the plasmonic excitation in a graphene nanodisk we simulated above.

By analogy to graphene nanodisk arrays, it is expected that such periodically conductivity modulated graphene nanodisks will show prominent optical absorption under far-field excitation, and the maximum absorption can be optimized by performing simulations and experiments for a series of such structures and adjusting the spacing of the conductivity modulated regions.

In the next chapter, we will discuss how this proposed structure can be experimentally realized. Specifically, we will present a geometry where Fermi level of an extended graphene sheet can be modulated independently in two different regions on a nanometer scale, using techniques that promise ultrahigh carrier densities.

Chapter 3

Nanoscale carrier density modulation of graphene with electrolyte gates and crosslinked-PMMA screens

In Chapter 2 we discussed graphene surface plasmonic modes in graphene nanostructures and their periodic arrays, with a focus on its implication in enhanced optical absorption in graphene thin films. The most promising structure proposed, nanoscale periodic conductivity modulation of a sheet of unpatterned graphene, shows prospects for enhanced optical absorption with lower damping rates and more effective and realistic graphene doping ability (Section 2.2.4). In this chapter, we present our experimental approach for realizing this proposed structure with electrolyte gates and crosslinked-PMMA screens.¹

We start by providing an overview of electrolytic gating of graphene, in which a comparison between electrolyte gates and traditional dielectrics such as SiO₂ will be made. We then proceed to our proposed electrolyte-PMMA-screen geometry. Primary components of the geometry will be illustrated and explained. In particular, the use of negative-tone crosslinked-PMMA as an electrolyte screening layer will be introduced and discussed. After that the effective functioning of the geometry will then be tested with a series of proof-of-principle measurements, including electrochemical, electrical

¹The author acknowledges collaboration with Dmitri Efetov on work presented in this chapter.

and optoelectronic testings. Finally, the fabrication technique of graphene devices with such electrolyte-PMMA-screen gates will be demonstrated. Sample devices with graphene plasmonic nanostructures realized by such geometry will be shown.

3.1 Electrolytic gating of graphene

As a 2D material, graphene's carrier density n can be readily changed electrostatically by inducing an electric field perpendicular to the graphene plane (the electric field effect (EFE)). This technique is effective for low-dimensional materials in general because the Debye screening length λ_D of accumulated charges is typically on the order of 10 nm and can penetrate the whole sample. It is also more flexible compared to another technique commonly used to dope graphene, chemical doping, because it allows *in situ* tuning of graphene's Fermi level which is essential for many applications including optical modulators, tunable spectral filters, optical switches and so on. Doping of graphene without the introduction of additional chemical dopants is also desirable since chemical dopants typically introduce additional disorder that prevents clean study of n -dependent physical properties.

Traditionally electrical gating of graphene and other semiconductor-based field effect transistors (FET) relies on thick (~ 300 nm) dielectrics such as SiO_2 , HfO_2 , and Al_2O_3 which are thermally grown or atomic-layer-deposited (ALD) on substrates such as highly doped silicon. A parallel-plate-capacitor model for such dielectrics is shown in Figure 3-1(a). A typical capacitance that can be achieved with this type of dielectrics is $C \sim 10$ nFcm⁻², which is limited by the dielectric break-down voltage of material with the given thickness. With a thickness of ~ 300 nm, the dielectric breaks down at voltages > 60 V accompanied by a discharge across the capacitor in the form of leakage currents. Decreasing the thickness of the dielectrics would result in higher capacitance, but also a lower break-down voltage. Hence, the highest carrier density induced with these dielectrics is typically $\sim 5 \times 10^{12}$ cm⁻²[15], corresponding to a graphene Fermi level of ~ 0.5 eV.

Electrolyte gates are an alternative to the traditional dielectric gates, and come

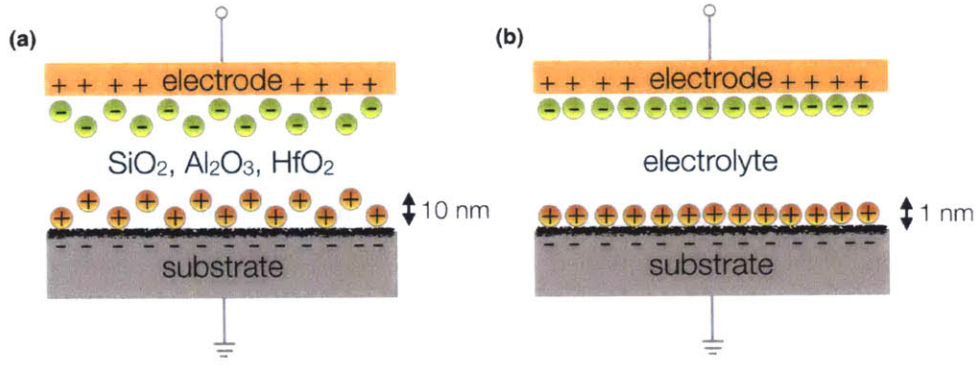


Figure 3-1: Parallel-plate-capacitor models of (a) traditional dielectric (SiO₂, HfO₂, and Al₂O₃) gates, and (b) electrolyte gates. The charges at the interfaces between the sample and the dielectric (electrolyte) schematically represents the Debye screening layer.

in various types and materials [57, 16, 64]. A parallel-plate-capacitor model for electrolyte gates is shown in Figure 3-1(b). As illustrated in the figure, the main difference between traditional dielectrics and electrolytes is that the Debye layer induced at the interface between the gated material and the electrolyte has a length d of only ~ 1 nm, while the corresponding length for traditional dielectrics is on the order of 10 nm. Therefore the resultant capacitances induced are much higher, reaching a value of $C \sim 5 \mu\text{Fcm}^{-2}$ [15], which is two orders of magnitude higher than capacitances typically achieved in traditional dielectrics. This small Debye length is a result of ionic charges accumulating in direct proximity to the gated material. The capacitance is again limited by the dielectric break-down voltage of the electrolyte material, which is normally accompanied by electrochemical reactions between the electrolyte and the gated sample. The highest reported carrier density induced in graphene with electrolyte gates is on the order of 10^{15} cm^{-2} [15], corresponding to a graphene Fermi level of ~ 1 eV.

3.2 Nanoscale electrolyte gates with electrolyte-PMMA-screen geometry

The proposed electrolyte-PMMA-screen geometry is illustrated in Figure 3-2. Large-area graphene (black) covers a doped Si substrate (dark gray) with a layer of HfO_2 or SiO_2 (light gray) grown on top. Above the graphene, a layer of crosslinked-PMMA (Poly(methyl methacrylate)) (purple) is defined with nanoscale structures. This PMMA layer serves as a screening layer for the solid polymer electrolyte gate (light blue) covering the entire sample. Metal (typically Au) (yellow) structures are defined to act as grounding (contacting) and gating electrodes.

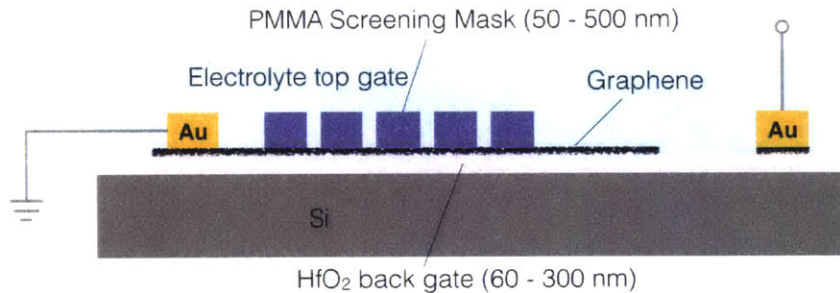


Figure 3-2: Schematic representation of a graphene device double gated with the proposed electrolyte-PMMA-screen geometry. Large-area graphene (black) covers a doped Si substrate (dark gray) with a layer of HfO_2 or SiO_2 (light gray) grown on top. Above the graphene, a layer of crosslinked-PMMA (Poly(methyl methacrylate)) (purple) is defined with nanoscale structures. This PMMA layer serves as a screening layer for the solid polymer electrolyte gate (light blue) covering the entire sample. Metal (typically Au) (yellow) structures are defined to act as grounding (contacting) and gating electrodes.

This geometry makes it possible to gate graphene independently and simultaneously in different regions, creating on-demand nanoscale carrier density modulation on a single sheet of extended graphene. From the “back”, graphene is globally gated with a dielectric backgate, giving a global doping and Fermi level across the entire graphene sheet; from the “top,” graphene is selectively gated with the electrolyte top gate in regions not covered with the crosslinked-PMMA screen, resulting in nanoscale local doping of graphene with respect to geometries defined with the PMMA screen.

Since the ultimate limit of resolution for the nanoscale gates depends on the resolution of the PMMA screen defined using electron beam (e-beam) lithography (which is < 10 nm [14]), and the Debye screening layer (~ 1 nm) is almost negligible compared to the nanostructure's feature size, the ultimate resolution for the nanoscale electrolyte gates produced by this geometry is < 10 nm. This grants us the capacity to fabricate nanostructures of arbitrary geometry, and the flexibility to tailor the size of the nanostructures such that the plasmonic resonant wavelength fits our application purposes. Furthermore, the inclusion of electrolytic gates promises reliable and effective doping of graphene into an ultrahigh carrier density regime of $n = 10^{15}$ cm $^{-2}$.

Poly(methyl methacrylate) (PMMA) has been used as an e-beam resist in nanotechnology [9, 4]. In most cases, it is used as a positive-tone resist, meaning that in the development process regions which have been exposed in electron beam dissolve in developers. On the other hand, when overexposed at a dose much higher than normal (~ 20000 $\mu\text{C}/\text{cm}^2$ as opposed to ~ 200 $\mu\text{C}/\text{cm}^2$), PMMA also exhibits a negative behavior. The resultant PMMA is crosslinked and transformed into carbon or graphitic nanostructures from a polymeric resist carbonization process [14, 13]. Sub-10-nm resolution has been achieved with e-beam lithography method, even at exposure energies as low as 2 keV [14]. Such material properties are suitable in particular for our proposed geometry, since high resolution of nanostructure is essential to produce graphene plasmonic resonances, and a good graphitic protection layer is desirable to prevent charged ions in the electrolyte top gate from leaking into the proximity of graphene. We note that a resist with those properties is not easily seen in the resist library. For example, the commonly used high-resolution negative resist HSQ is a good candidate for sub-10-nm fine structures; however, it provides poor protection when it comes to prevention of charged ions from penetrating the layer.

An example of exposed and developed negative-tone crosslinked-PMMA (from now on we refer to it as PMMA for simplicity) on Si substrate is shown in Figure 3-3. The sample is fabricated using the Raith 150 electron beam lithography system at an electron acceleration voltage of 30 keV and a dose in the range of 7000-30000 $\mu\text{C}/\text{cm}^2$, using a 950 PMMA layer of thickness 200 nm. The optical image on the left illustrates

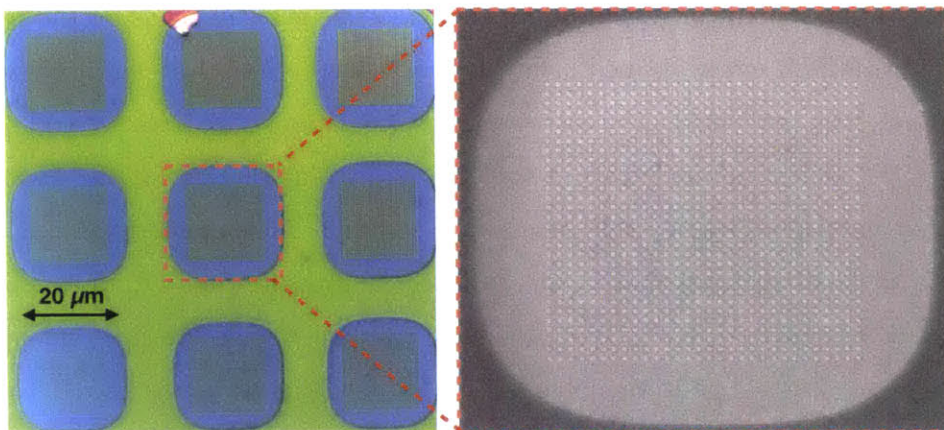


Figure 3-3: Optical (left) and scanning-electron-microscopy (SEM) (right) images of exposed and developed negative-tone cross-linked PMMA nanostructures on Si substrate, fabricated with Raith 150 system at MIT at 30 keV using 200-nm-thick PMMA. The overexposed PMMA circles has a radius of 100 nm, and a lattice constant of 400 nm. Yellow dots: overexposed PMMA circles; blue: PMMA exposed at a normal dose due to electron diffusion; green: unexposed PMMA.

PMMA exposed at three different characteristic doses: in the center (yellow dots), PMMA is overexposed to define graphitic nanodisks of radius 100 nm; around the center region (blue), due to electron diffusion, PMMA is exposed at a normal dose so has been dissolved in the developer in the development process; away from the directly exposed center region, PMMA is not exposed to e-beam, so remains on the substrate after development. The remaining unexposed PMMA can be readily removed by acetone. The scanning-electron-micrograph (SEM) on the right demonstrates our ability to define nanostructures using negative-tone cross-linked PMMA.

3.3 Proof-of-principle testings of electrolyte-PMMA-screen gates

In this section we present a series of proof-of-principle testings of the proposed electrolyte-PMMA-screen geometry, including electrochemical, electrical and optoelectronic measurements. These characterizations of the proper functioning of the proposed geometry and fabricated devices are necessary prerequisites for applying

this method to produce nanoscale periodic conductivity modulation in graphene for infrared plasmonics.

3.3.1 Protection from charge leaking through PMMA screens

The electric field effect produced in the proximity of graphene by electrolyte stems from charged ions that accumulate close to the interface between electrolyte and the gated material. The electrolyte of our choice consists of the polymer (ethylene)oxide (PEO) and the salt lithium perchlorate (LiClO_4). Upon mixing with each other, PEO acts as a solvent of LiClO_4 and separates it into charged Li^+ and ClO_4^- ions. This is illustrated in Figure 3-4. We note that although Li^+ is highly reactive and

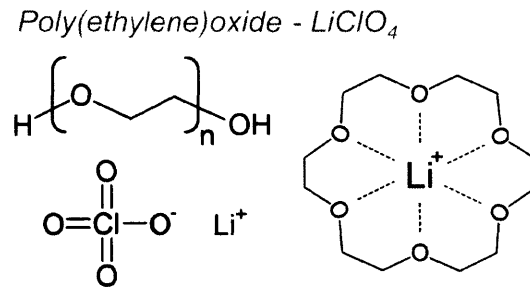


Figure 3-4: Chemical composition of the polymer (ethylene)oxide (PEO) and the salt lithium perchlorate (LiClO_4) (left). Upon dissolving LiClO_4 in the solvent PEO, LiClO_4 is separated into charged ions Li^+ and ClO_4^- . The highly reactive Li^+ is wrapped in PEO chains, thus protected from chemical reactions with the environment. From [15].

can potentially be involved in chemical reactions that modify surface properties of the sample, it is actually wrapped in PEO chains (shown in Figure 3-4 on the right), which protects it from reacting with its environment. This electrolyte greatly enhances the voltage that can be applied to the electrolyte gate before it breaks down.

To make sure the electric field effect of the nanoscale electrolyte gates shares the same spatial profile as the PMMA nanostructures used to define the gates, the charged ions should spatially be distributed along the interface between the PMMA screen and the electrolyte. Due to the mobile nature of the charged ions, one concern is that the ions might leak through the PMMA screen, destroying the nanostructure-defined

electrostatic profile. In this section, we demonstrate that the crosslinked-PMMA screen provides a good protection from charge leaking from the electrolyte.

As mentioned in Section 3.1, when applying a voltage greater than the breakdown voltage (typically ~ 5 V) of the electrolyte gate, chemical reactions happen between electrolyte and the gated material, severely modify the interface between the materials, potentially resulting in an insulating sacrificial layer that prevents charged ions from gating the sample, causing a largely reduced resultant capacitance. Most of the time, these chemical reactions are visible by the eyes, and one can easily recognize when the applied voltage starts to cause the electrolyte and the sample to degrade. We therefore make use of this visible degradation phenomenon to guide us in determining whether charged ions from the electrolyte can diffuse through the PMMA screen and reach the graphene surface.

The control experimental scheme is shown in Figure 3-5(a). PMMA screen squares

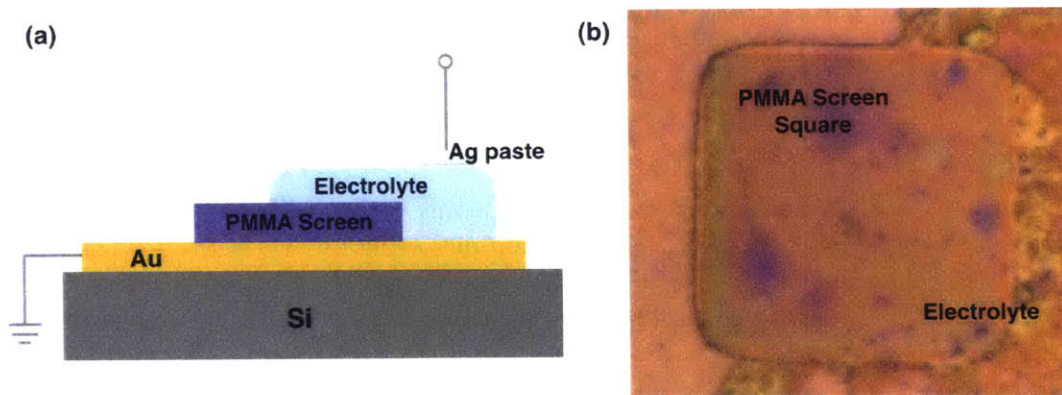


Figure 3-5: Experimental scheme and the result for testing the impenetrability of PMMA screens for charged ions from electrolyte gates. The tested Au electrode is partially covered by a PMMA screen square. Voltage is applied to a global electrolyte gate covering both areas. After a high voltage ($V > V_{break-down}$) is applied, exposed area of the electrode suffer from severe corrosion whereas protected area of the electrode remain intact.

are defined on top of a Au electrode previously patterned on a Si substrate. This electrode serves as the grounding electrode. Freshly mixed PEO-LiClO₄ electrolyte is then dip-dropped onto the Au electrode which is partly protected by the PMMA square. Silver paste is then deposited onto the electrolyte, acting as a top gating

electrode. Electric voltage is then applied to the structure. At low gating voltages ($V_{eg} < 5$ V), no chemical reactions and sample degradation are observed; starting from $V_{eg} \simeq 6$ V, visible signs of chemical reactions between electrolyte and the Au electrode start to show up in regions not covered by the PMMA screen. The electrolyte is removed after applying such voltage for a while. As shown in Figure 3-5(b), the exposed Au surface seems to have suffered from strong corrosion, whereas the Au area that is protected by the PMMA shows no signatures of corrosion or pin holes that are typically observed in degraded electrolyte samples. This is showing that charged ions in electrolyte have not managed to penetrate the PMMA screen and reach the electrode surface for chemical reactions to happen. From this we conclude that the PMMA screen protects the substrate and maintains the spatial profile of the charged ions defined by the PMMA nanostructures. Thus, we expect the electrostatic profile to duplicate the spatial profile of the patterned PMMA nanostructure, creating the nanoscale electrolyte gates as we desire.

3.3.2 Resistance measurement of a graphene p - n junction

We then characterize the electrolyte-PMMA-screen geometry electrically to test the modulation capacity of graphene samples' doping and Fermi level with the electrolyte gate. We demonstrate that local carrier density modulation is achievable, where an extended sheet of graphene is doped to different Fermi levels spatially according to a PMMA-defined screening mask.

A typical graphene FET device with a local electrolyte top gate is shown in Figure 3-6(b). This device is fabricated with the large-scale CVD graphene manufacturing technique that we developed in our group. An example of a typical chip produced using such technique is shown in Figure 3-6(a). The detailed fabrication method will be the topic for Section 3.4.1. As shown in Figure 3-6(a)(b), the device consists of two contacting electrodes with a graphene channel (indicated by black dash line) in between. Two large Au pads on the side of the graphene serve as the gating electrode for electrolyte gate. The yellow square covering half of the graphene channel is a layer of PMMA screen. Electrolyte is deposited on the entire device after the device

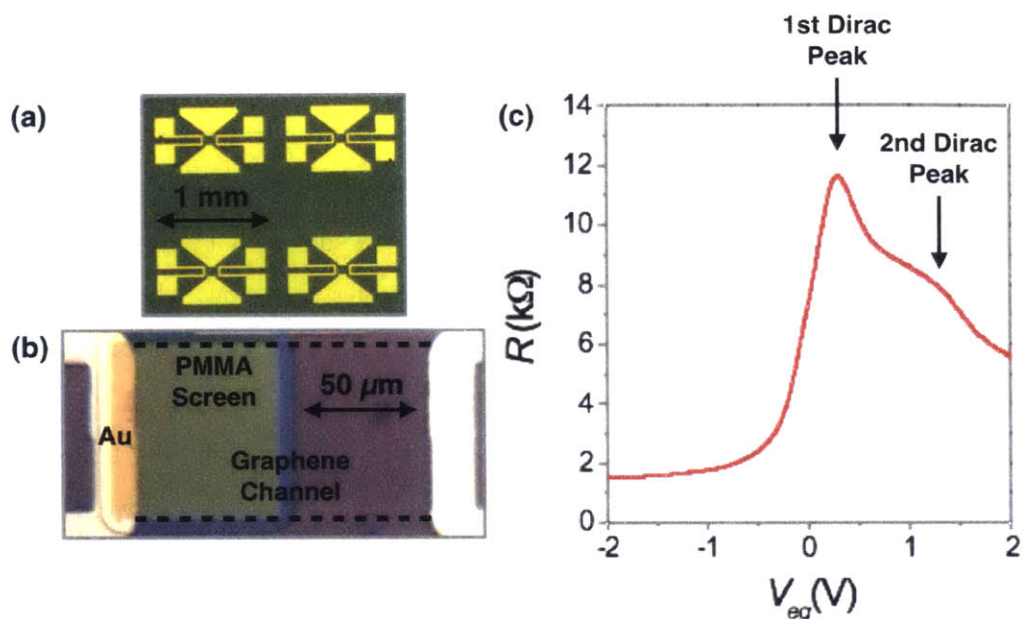


Figure 3-6: Electrical measurement of a graphene p - n junction. (a) Optical image of an example of fabricated large-scale CVD graphene devices. (b) Optical image of a graphene FET device consisting of contacting and gating electrodes, with an electrolyte-PMMA-screen local gate on top. Half of the graphene channel is covered by the PMMA screen. Electrolyte is not shown in this picture. (c) Resistance of the device as a function of applied electrolyte gate voltage V_{eg} under ambient conditions.

is fabrication (electrolyte not shown in the picture). (Note: the picture shows the device before unexposed PMMA is removed.)

Under ambient conditions, the electrolyte gate voltage V_{eg} is applied to the sample and swept continuously from $V_{eg} = -2$ V to $V_{eg} = 2$ V. The resultant charged ion layers in the proximity of graphene surface dope the graphene channel to, p -type (left), undoped (Dirac peak), or n -type (right) regimes. Figure 3-6(c) shows the resistance of the graphene channel as a function of the applied electrolyte gate voltage V_{eg} ; it illustrates graphene's changing of doping level as a result of electrolyte. Different from typical resistance characteristics of graphene FETs [11], here the resistance curve shows two characteristic Dirac peaks. This is expected because the graphene channel is partially covered with a PMMA screening mask, which effectively causes the channel to be split into two regions with different carrier densities. The measured resistance can be regarded as the sum of the resistances of the two regions. Due to the difference

in carrier densities, the Dirac peak shows up at different gating voltages $V_{eg,1}$ and $V_{eg,2}$. The sum of the resistance curves thus exhibits two Dirac peaks, as what we observed in the resistance measurement of the prepared electrolyte-PMMA-screen device.

We note that there is an asymmetry in the resistance curve between negative and positive gate voltages. This asymmetry of the base line comes from the difference in mobility of electrons and holes at the interface formed by graphene and the metal contact [29]. The second Dirac peak has a larger FWHM compared to the first one because the PMMA mask on top of the graphene lowers the carrier mobility compared to “cleaner” graphene.

3.3.3 Photocurrent measurement of a series of graphene p - n junctions

The electrical measurement we present in the above section provides initial evidence on the selective gating of graphene with the proposed electrolyte-PMMA-screen geometry. In this section we demonstrate a further confirmation of the desirable selective local carrier density modulation using photocurrent measurements. Spatial mapping of the photocurrent provides us with insights on spatial variation of graphene carrier densities generated with the electrolyte-PMMA-screen local gates.

The photocurrent generated in our graphene device is likely primarily generated through the photo-thermoelectric (PTE) effect [53]. The mechanism can be understood as follows: a laser spot is incident on a graphene region, generating hot carriers and creating a temperature gradient as it is absorbed in graphene. If this temperature gradient is overlapped with a p - n junction, the difference in Seebeck coefficient of the p - and n - regions would result in a photocurrent, which can be written as [53]

$$I_{ph} = \frac{s_1 - s_2}{R} \Delta T \quad (3.1)$$

where R is the resistance of the graphene sheet under excitation, ΔT is the temper-

ature gradient, and s_1, s_2 are Seebeck coefficients that are expressed as [53]

$$s(\mu) = -\frac{\pi^2 k_B^2 T}{3e} \frac{1}{\sigma} \frac{d\sigma}{d\mu} \quad (3.2)$$

We note the dependence of the Seebeck coefficient on the conductivity of graphene, which is the reason why typically PTE is induced on graphene p - n junctions.

Figure 3-7(a) shows a graphene FET device fabricated in the same way as the above device used for electrical measurements. Instead of a single PMMA-screen

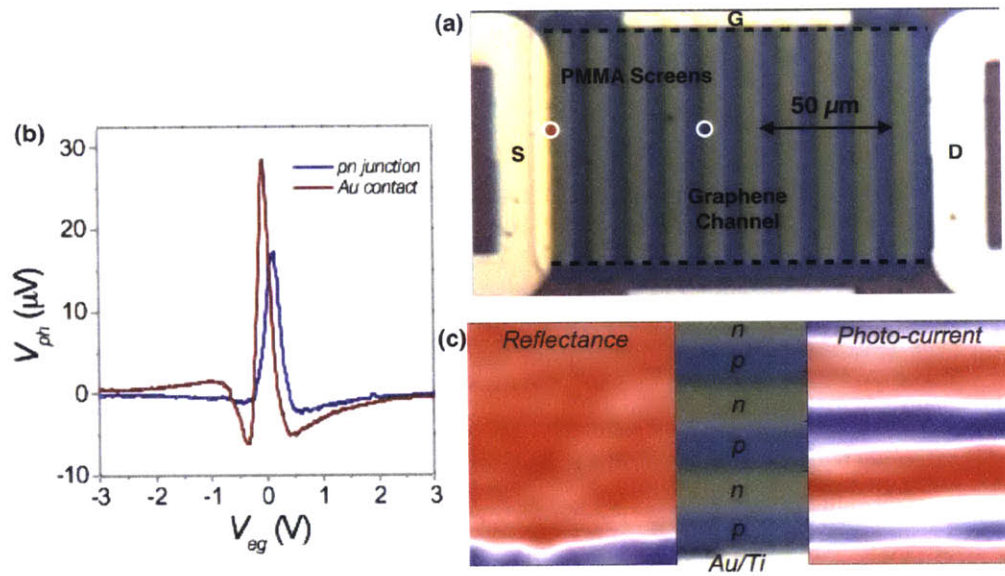


Figure 3-7: Optoelectronic measurements of a series of graphene p - n junctions. (a) Optical image of a graphene FET device consisting of contacting and gating electrodes, with a series of electrolyte-PMMA-screen local gates on top. The graphene channel is covered by a series of PMMA strips that are $5 \mu\text{m}$ in width. Electrolyte is not shown in this picture. (b) Photocurrent generated in the device as a function of applied electrolyte gate voltage V_{eg} under ambient conditions. Two spatial locations are measured: blue: a p - n junction formed in the middle of the graphene channel; red: the interface between graphene and the metal contact. The locations are indicated with colored dots in (a). (c) Photocurrent spatial mapping and the reflectance mapping of the graphene channel, aligned with the optical image of the device. Colors in the photocurrent mapping denotes photocurrent direction and magnitude; colors in the reflectance mapping denotes reflected power. A laser at wavelength $\lambda = 1550 \text{ nm}$ with a spot size of $\sim 3 \mu\text{m}$, modulated at 100 Hz , is used to excite the photocurrent.

square that defines a single p - n junction in the graphene channel, this device is covered

with a series of PMMA-screen strips, resulting in a series of p - n junctions across the graphene channel.

The photocurrent generation through PTE is first demonstrated and compared with the previously investigated PTE at the interface between graphene and a metal contact [52]. We measured the photocurrent as a function of the applied electrolyte gate voltage V_{eg} at two locations indicated by the two colored dots in Figure 3-7(a), one at the graphene-contact interface, the other at a p - n junction created by the electrolyte-PMMA-screen gate in the middle of the graphene channel. As the applied electrolyte gate voltage V_{eg} is swept from $V_{eg} = -3$ V to $V_{eg} = 3$ V, the photocurrent undergoes a 3-fold sign change at both locations, as expected from PTE [52], confirming the same photocurrent generation mechanism of the two locations. The “Fermi level pinning” effect of the metal contact is essentially the change of the graphene’s doping level to form a p - n junction at the interface. Hence we conclude that our electrolyte-PMMA-screen local gate is successful in creating such p - n junction as well.

Finally we perform a spatial photocurrent mapping of the graphene channel to get an idea of the spatial profile of the graphene carrier density modulated by the electrolyte-PMMA-screen local gates. Figure 3-7(c) shows the spatial reflectance mapping and the spatial photocurrent mapping of the graphene channel, aligned to the optical image of the device. The blue color in the reflectance mapping corresponds to the prominent reflection from the metal contact. The color in the photocurrent mapping denotes the magnitude and direction of the photocurrent. As expected, the photocurrent is primarily generated at the interface between different carrier density regions, where the direction of the photocurrent generated at a p - n interface is opposite to the direction of the photocurrent generated at a n - p interface. The locations of the interfaces and the maximum photocurrent locations are in good agreement. This photocurrent mapping again confirms the p - n junction formation by the electrolyte-PMMA-screen; in addition, it shows that the spatial profile of the graphene carrier density is indeed defined by the local gates we patterned on top of the graphene channel.

This concludes the proof-of-principle testings of our proposed electrolyte-PMMA-screen gate geometry. All the electrochemical, electrical and optoelectronic measurements confirm the exceptional ability of this geometry to generate effective and reliable spatial carrier density modulation of graphene on a nanometer scale, which is essential for our future study of infrared plasmonic modes in graphene nanostructures.

3.4 Fabrication technique for electrolyte-PMMA-screen gates

3.4.1 Large-scale fabrication procedures

The manufacturing technique for graphene devices with electrolyte-PMMA-screen gates is illustrated in Figure 3-8. We note that this fabrication technique is extremely

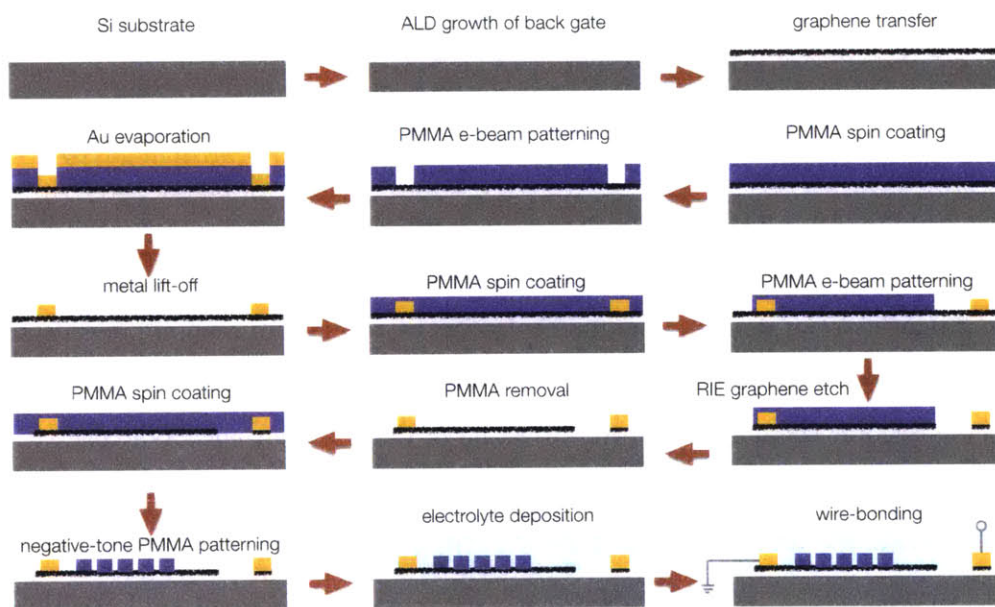


Figure 3-8: Illustration of fabrication technique for CVD graphene devices with electrolyte-PMMA-screen gates. Color: dark gray: Si substrate; light gray: back gate dielectric; thick black line: graphene; purple: PMMA; gold: Au; light blue: electrolyte; gray line: wire bonds.

efficient and flexible. Large-area CVD graphene is used, so in each entire fabrication

run, close to 50 devices can be fabricated. And all processing steps involved can be scaled to manufacture devices from nanometer to micrometer scale, granting us with the flexibility to fabricate all sorts of potential devices in which spatial carrier density modulation of graphene and beyond is desirable. One can expect the same technique to be applied to, for example, other 2D materials such as MoS₂, WSe₂, or topological insulators, where on-demand doping of the materials is called for.

3.4.2 Graphene devices with nanoscale carrier density modulation gates

In Figure 3-9 we show some example devices that have been fabricated with the procedure illustrated above. The scale of the devices shown range from nanometer to micrometer; the PMMA screens patterned show a variety of geometries; and the applications of the devices include graphene plasmonic nanostructures, graphene photodetection in the infrared wavelength, and beyond:

- **(a)** Graphene plasmonic nanostructures with nanoscale spatial conductivity modulation. Conductivity-modulated disks have radius $r = 50$ nm.
- **(b)** Graphene plasmonic nanostructures with nanoscale spatial conductivity modulation. Conductivity-modulated ribbons have width $d = 100$ nm.
- **(c)** Graphene devices we used to perform proof-of-principle testings of electrolyte-PMMA-screen geometry. Width of strips is $d = 5$ μm . Side length of squares is $a = 5$ μm .

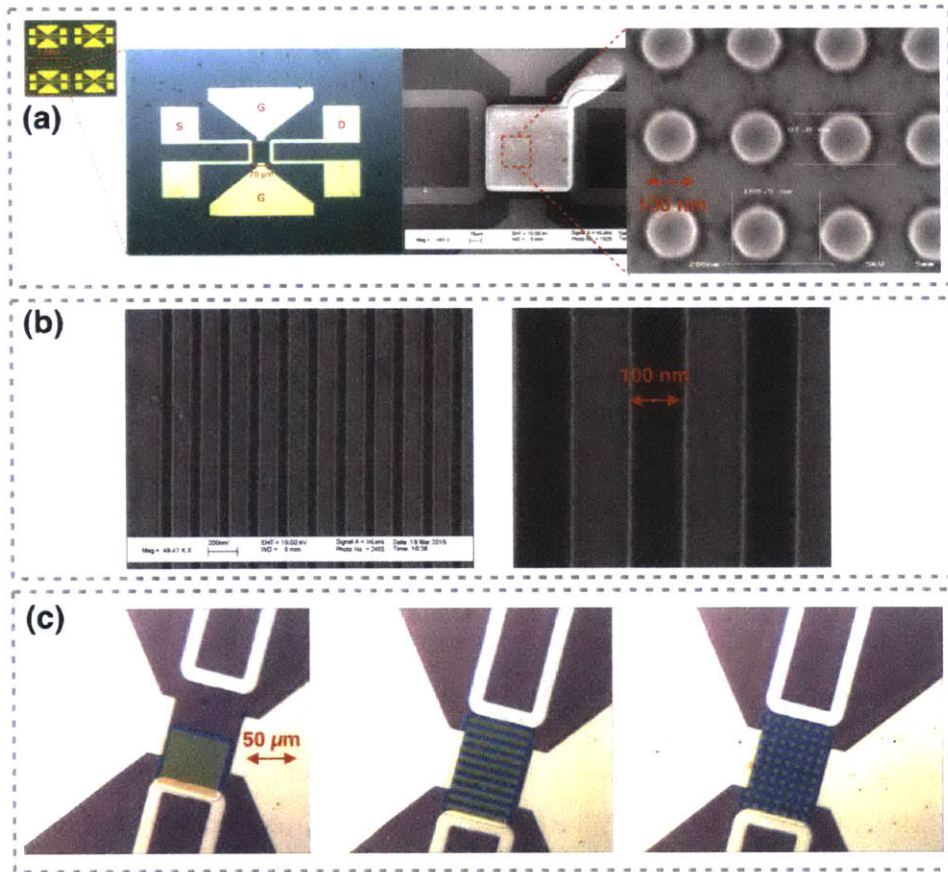


Figure 3-9: Examples of graphene devices with electrolyte-PMMA-screen gates fabricated using procedures illustrated in Section 3.4.1.

Chapter 4

Conclusion and outlook

In this thesis we demonstrated graphene plasmonic modes in graphene nanostructures and their periodic arrays. Simulations and theoretical calculations showed that the extreme confinement of light in such structures results in strongly enhanced (and even perfect) optical absorption in the periodic nanostructure arrays. In addition, the resonant plasmonic excitations can be tuned *in situ* in wavelength with electrical gating, which is highly desirable in a number of active optoelectronic applications such as tunable filters and optical switches.

In light of the simulation and theoretical results, we have proposed an experimental approach, the electrolyte-PMMA-screen geometry, to realize such plasmonic modes in an extended sheet of graphene, whose carrier density is periodically modulated on a nanometer scale. The proper functioning of the proposed approach has been proven with a series of proof-of-principle measurements, and the fabrication of such structures has been illustrated. This experimental technique can also be applied to a variety of other 2D materials to create local carrier density modulations in arbitrary geometries on demand, opening up possibilities for numerous potential applications in the field of optoelectronics and beyond.

Finally, we provide an outlook of future studies in the field of infrared plasmonics following the completion of this thesis. To begin with, we will be testing the performance of the graphene nanostructures designed and fabricated with our electrolyte-PMMA-screen technique. Mid-infrared absorption/transmission spectroscopy will be

used to characterize the optical absorption of the graphene thin film, and the mid-IR characterization setup is currently under construction in our lab.

In addition to exciting graphene plasmons with periodic nanostructures, the ability to excite plasmonic modes in structures such as a single nanodisk is also desirable, with applications such as single-photon optical switches [26] in mind. This has long been a problem in the field of plasmonics due to the large wave-vector mismatch between plasmons and free-space light, and various approaches have been proposed to increase the coupling efficiency, including scanning type near-field optical microscope (s-SNOM) [8, 21], surface acoustic wave mediation [50], dielectric gratings [65, 67], and difference frequency generation [10], to name a few. However, the coupling efficiency between plasmons and photons has not been satisfactory. To this end, we are thinking about solving this plasmon-free-space coupling problem with solid-state cavity electrodynamics (QED). By making use of geometries such as Bull’s eye cavities and one-dimensional nanobeam cavities, shown in Figure 4-1, one can combine the phase-matching advantages of dielectric grating couplers with the field enhancement advantage of a dielectric cavity to simultaneously achieve free-space-plasmon coupling and further boost optical field enhancement.

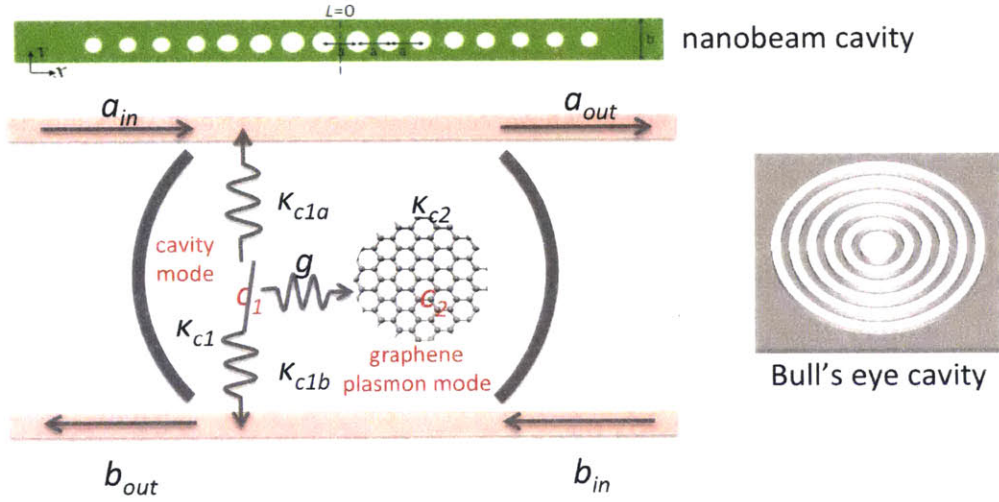


Figure 4-1: Coupling between free-space (or wave-guided) mode and graphene plasmonic mode. The coupled mode theory picture of the scheme along with two cavity geometries under consideration are presented. Picture of the nanobeam cavity is from [47]; picture of the bull’s eye cavity is from [51].

Bibliography

- [1] Graphene's lattice structure in k-space and dirac cones at k and k' points. <http://www.mpipks-dresden.mpg.de/mpi-doc/CondensedMatter/media/scientific/honeylattice.png>. Accessed May 12, 2014.
- [2] Scuff-em: Free, open-source software for boundary-element analysis of problems in computational physics and engineering. <http://homerreid.com/scuff-EM>. Accessed Aug 28, 2015.
- [3] Qiaoliang Bao and Kian Ping Loh. Graphene photonics, plasmonics, and broadband optoelectronic devices. *ACS nano*, 6(5):3677–3694, 2012.
- [4] SP Beaumont, PG Bower, T Tamamura, and CDW Wilkinson. Sub-20-nm-wide metal lines by electron-beam exposure of thin poly (methyl methacrylate) films and liftoff. *Applied Physics Letters*, 38(6):436–439, 1981.
- [5] László P Biró, Péter Nemes-Incze, and Philippe Lambin. Graphene: nanoscale processing and recent applications. *Nanoscale*, 4(6):1824–1839, 2012.
- [6] Francesco Bonaccorso, Z Sun, T Hasan, and AC Ferrari. Graphene photonics and optoelectronics. *Nature photonics*, 4(9):611–622, 2010.
- [7] DE Chang, Anders Søndberg Sørensen, PR Hemmer, and MD Lukin. Quantum optics with surface plasmons. *Physical review letters*, 97(5):053002, 2006.
- [8] Jianing Chen, Michela Badioli, Pablo Alonso-González, Sukosin Thongrattanasiri, Florian Huth, Johann Osmond, Marko Spasenović, Alba Centeno, Amaia Pesquera, Philippe Godignon, et al. Optical nano-imaging of gate-tunable graphene plasmons. *Nature*, 487(7405):77–81, 2012.
- [9] Wei Chen and Haroon Ahmed. Fabrication of 5–7 nm wide etched lines in silicon using 100 keV electron-beam lithography and polymethylmethacrylate resist. *Applied physics letters*, 62(13):1499–1501, 1993.
- [10] Thomas J Constant, Samuel M Hornett, Darrick E Chang, and Euan Hendry. All-optical generation of surface plasmons in graphene. *arXiv preprint arXiv:1505.00127*, 2015.
- [11] Anindya Das, S Pisana, B Chakraborty, S Piscanec, SK Saha, UV Waghmare, KS Novoselov, HR Krishnamurthy, AK Geim, AC Ferrari, et al. Monitoring

- dopants by raman scattering in an electrochemically top-gated graphene transistor. *Nature nanotechnology*, 3(4):210–215, 2008.
- [12] FJ García De Abajo. Colloquium: Light scattering by particle and hole arrays. *Reviews of Modern Physics*, 79(4):1267, 2007.
- [13] HG Duan, EQ Xie, and L Han. Turning electrospun poly (methyl methacrylate) nanofibers into graphitic nanostructures by in situ electron beam irradiation. *Journal of Applied Physics*, 103(4):046105, 2008.
- [14] Huigao Duan, Donald Winston, Joel KW Yang, Bryan M Cord, Vitor R Manfrinato, and Karl K Berggren. Sub-10-nm half-pitch electron-beam lithography by using poly (methyl methacrylate) as a negative resist. *Journal of Vacuum Science & Technology B*, 28(6):C6C58–C6C62, 2010.
- [15] Dmitri K Efetov. *Towards inducing superconductivity into graphene*. PhD thesis, Columbia University, 2014.
- [16] Dmitri K Efetov and Philip Kim. Controlling electron-phonon interactions in graphene at ultrahigh carrier densities. *Physical review letters*, 105(25):256805, 2010.
- [17] LA Falkovsky. Optical properties of graphene. In *Journal of Physics: Conference Series*, volume 129, page 012004. IOP Publishing, 2008.
- [18] Zheyu Fang, Sukosin Thongrattanasiri, Andrea Schlather, Zheng Liu, Lulu Ma, Yumin Wang, Pulickel M Ajayan, Peter Nordlander, Naomi J Halas, and F Javier García de Abajo. Gated tunability and hybridization of localized plasmons in nanostructured graphene. *ACS nano*, 7(3):2388–2395, 2013.
- [19] Zheyu Fang, Yumin Wang, Zheng Liu, Andrea Schlather, Pulickel M Ajayan, Frank HL Koppens, Peter Nordlander, and Naomi J Halas. Plasmon-induced doping of graphene. *Acs Nano*, 6(11):10222–10228, 2012.
- [20] Zheyu Fang, Yumin Wang, Andrea E Schlather, Zheng Liu, Pulickel M Ajayan, F Javier García de Abajo, Peter Nordlander, Xing Zhu, and Naomi J Halas. Active tunable absorption enhancement with graphene nanodisk arrays. *Nano letters*, 14(1):299–304, 2013.
- [21] Zhe Fei, AS Rodin, GO Andreev, W Bao, AS McLeod, M Wagner, LM Zhang, Z Zhao, M Thiemens, G Dominguez, et al. Gate-tuning of graphene plasmons revealed by infrared nano-imaging. *Nature*, 487(7405):82–85, 2012.
- [22] Xuetao Gan, Kin Fai Mak, Yuanda Gao, Yumeng You, Fariba Hatami, James Hone, Tony F Heinz, and Dirk Englund. Strong enhancement of light-matter interaction in graphene coupled to a photonic crystal nanocavity. *Nano letters*, 12(11):5626–5631, 2012.

- [23] Xuetao Gan, Ren-Jye Shiue, Yuanda Gao, Inanc Meric, Tony F Heinz, Kenneth Shepard, James Hone, Solomon Assefa, and Dirk Englund. Chip-integrated ultra-fast graphene photodetector with high responsivity. *Nature Photonics*, 7(11):883–887, 2013.
- [24] F Javier Garcia de Abajo. Graphene plasmonics: challenges and opportunities. *Acs Photonics*, 1(3):135–152, 2014.
- [25] AN Grigorenko, Marco Polini, and KS Novoselov. Graphene plasmonics. *Nature photonics*, 6(11):749–758, 2012.
- [26] M Gullans, DE Chang, FHL Koppens, FJ García de Abajo, and Mikhail D Lukin. Single-photon nonlinear optics with graphene plasmons. *Physical review letters*, 111(24):247401, 2013.
- [27] Y Hadad and Ben Z Steinberg. Quasistatic resonance of a chemical potential interruption in a graphene layer and its polarizability: The mixed-polarity semilocalized plasmon. *Physical Review B*, 88(7):075439, 2013.
- [28] Euan Hendry, Peter J Hale, Julian Moger, AK Savchenko, and SA Mikhailov. Coherent nonlinear optical response of graphene. *Phys. Rev. Lett*, 105(9):097401, 2010.
- [29] B Huard, N Stander, JA Sulpizio, and D Goldhaber-Gordon. Evidence of the role of contacts on the observed electron-hole asymmetry in graphene. *Physical Review B*, 78(12):121402, 2008.
- [30] EH Hwang and S Das Sarma. Dielectric function, screening, and plasmons in two-dimensional graphene. *Physical Review B*, 75(20):205418, 2007.
- [31] Marinko Jablan and Darrick E Chang. Multi-plasmon absorption in graphene. *arXiv preprint arXiv:1501.05258*, 2015.
- [32] Min Seok Jang, Victor W Brar, Michelle C Sherrott, Josue J Lopez, Laura Kim, Seyoon Kim, Mansoo Choi, Harry A Atwater, et al. Tunable large resonant absorption in a midinfrared graphene salisbury screen. *Physical Review B*, 90(16):165409, 2014.
- [33] Long Ju, Baisong Geng, Jason Horng, Caglar Girit, Michael Martin, Zhao Hao, Hans A Bechtel, Xiaogan Liang, Alex Zettl, Y Ron Shen, et al. Graphene plasmonics for tunable terahertz metamaterials. *Nature nanotechnology*, 6(10):630–634, 2011.
- [34] Frank HL Koppens, Darrick E Chang, and F Javier Garcia de Abajo. Graphene plasmonics: a platform for strong light–matter interactions. *Nano letters*, 11(8):3370–3377, 2011.
- [35] Zhaoyi Li and Nanfang Yu. Modulation of mid-infrared light using graphene-metal plasmonic antennas. *Applied Physics Letters*, 102(13):131108, 2013.

- [36] ZQ Li, Eric A Henriksen, Z Jiang, Zhao Hao, Michael C Martin, P Kim, HL Stormer, and Dimitri N Basov. Dirac charge dynamics in graphene by infrared spectroscopy. *Nature Physics*, 4(7):532–535, 2008.
- [37] Stephan Link and Mostafa A El-Sayed. Size and temperature dependence of the plasmon absorption of colloidal gold nanoparticles. *The Journal of Physical Chemistry B*, 103(21):4212–4217, 1999.
- [38] Yu Liu, RF Willis, KV Emtsev, and Th Seyller. Plasmon dispersion and damping in electrically isolated two-dimensional charge sheets. *Physical Review B*, 78(20):201403, 2008.
- [39] Tony Low and Phaedon Avouris. Graphene plasmonics for terahertz to mid-infrared applications. *Acs Nano*, 8(2):1086–1101, 2014.
- [40] Kin Fai Mak, Matthew Y Sfeir, Yang Wu, Chun Hung Lui, James A Misewich, and Tony F Heinz. Measurement of the optical conductivity of graphene. *Physical review letters*, 101(19):196405, 2008.
- [41] Xiaochang Miao, Sefaattin Tongay, Maureen K Petterson, Kara Berke, Andrew G Rinzler, Bill R Appleton, and Arthur F Hebard. High efficiency graphene solar cells by chemical doping. *Nano letters*, 12(6):2745–2750, 2012.
- [42] Gustav Mie. Beiträge zur optik trüber medien, speziell kolloidaler metallösungen. *Annalen der physik*, 330(3):377–445, 1908.
- [43] Shuming Nie and Steven R Emory. Probing single molecules and single nanoparticles by surface-enhanced raman scattering. *science*, 275(5303):1102–1106, 1997.
- [44] A Yu Nikitin, F Guinea, FJ García-Vidal, and Luis Martín-Moreno. Edge and waveguide terahertz surface plasmon modes in graphene microribbons. *Physical Review B*, 84(16):161407, 2011.
- [45] A Yu Nikitin, F Guinea, FJ Garcia-Vidal, and Luis Martin-Moreno. Surface plasmon enhanced absorption and suppressed transmission in periodic arrays of graphene ribbons. *Physical Review B*, 85(8):081405, 2012.
- [46] KSA Novoselov, Andre K Geim, SVb Morozov, Da Jiang, MIc Katsnelson, IVa Grigorieva, SVb Dubonos, and AAb Firsov. Two-dimensional gas of massless dirac fermions in graphene. *nature*, 438(7065):197–200, 2005.
- [47] Qimin Quan and Marko Loncar. Deterministic design of wavelength scale, ultra-high q photonic crystal nanobeam cavities. *Optics express*, 19(19):18529–18542, 2011.
- [48] MT Reid and Steven G Johnson. Efficient computation of power, force, and torque in bem scattering calculations. *arXiv preprint arXiv:1307.2966*, 2013.

- [49] Jeremy T Robinson, F Keith Perkins, Eric S Snow, Zhongqing Wei, and Paul E Sheehan. Reduced graphene oxide molecular sensors. *Nano letters*, 8(10):3137–3140, 2008.
- [50] C Ruppert, J Neumann, JB Kinzel, HJ Krenner, A Wixforth, and M Betz. Surface acoustic wave mediated coupling of free-space radiation into surface plasmon polaritons on plain metal films. *Physical Review B*, 82(8):081416, 2010.
- [51] Jacob Scheuer, William MJ Green, and Amnon Yariv. Annular bragg resonators (abr): the ideal tool for biochemical sensing, nonlinear optics, and cavity qed. In *Integrated Optoelectronic Devices 2006*, pages 61230S–61230S. International Society for Optics and Photonics, 2006.
- [52] Ren-Jye Shiue, Yuanda Gao, Yifei Wang, Cheng Peng, Alexander D Robertson, Dimitri Efetov, Solomon Assefa, Frank HL Koppens, James Hone, and Dirk Englund. High-responsivity graphene-boron nitride photodetector and autocorrelator in a silicon photonic integrated circuit. *arXiv preprint arXiv:1507.00426*, 2015.
- [53] Justin CW Song, Mark S Rudner, Charles M Marcus, and Leonid S Levitov. Hot carrier transport and photocurrent response in graphene. *Nano letters*, 11(11):4688–4692, 2011.
- [54] Frank Stern. Polarizability of a two-dimensional electron gas. *Physical Review Letters*, 18(14):546, 1967.
- [55] Sukosin Thongrattanasiri, Frank HL Koppens, and F Javier García de Abajo. Complete optical absorption in periodically patterned graphene. *Physical review letters*, 108(4):047401, 2012.
- [56] Sukosin Thongrattanasiri, Alejandro Manjavacas, and F Javier García de Abajo. Quantum finite-size effects in graphene plasmons. *Acs Nano*, 6(2):1766–1775, 2012.
- [57] K Ueno, S Nakamura, H Shimotani, A Ohtomo, N Kimura, T Nojima, H Aoki, Y Iwasa, and M Kawasaki. Electric-field-induced superconductivity in an insulator. *Nature materials*, 7(11):855–858, 2008.
- [58] Xuan Wang, Linjie Zhi, and Klaus Müllen. Transparent, conductive graphene electrodes for dye-sensitized solar cells. *Nano letters*, 8(1):323–327, 2008.
- [59] Paul R West, Satoshi Ishii, Gururaj V Naik, Naresh K Emani, Vladimir M Shalaev, and Alexandra Boltasseva. Searching for better plasmonic materials. *Laser & Photonics Reviews*, 4(6):795–808, 2010.
- [60] B Wunsch, T Stauber, F Sols, and F Guinea. Dynamical polarization of graphene at finite doping. *New Journal of Physics*, 8(12):318, 2006.

- [61] Hugen Yan, Xuesong Li, Bhupesh Chandra, George Tulevski, Yanqing Wu, Marcus Freitag, Wenjuan Zhu, Phaedon Avouris, and Fengnian Xia. Tunable infrared plasmonic devices using graphene/insulator stacks. *Nature Nanotechnology*, 7(5):330–334, 2012.
- [62] Hugen Yan, Tony Low, Wenjuan Zhu, Yanqing Wu, Marcus Freitag, Xuesong Li, Francisco Guinea, Phaedon Avouris, and Fengnian Xia. Damping pathways of mid-infrared plasmons in graphene nanostructures. *Nature Photonics*, 7(5):394–399, 2013.
- [63] Yu Yao, Raji Shankar, Patrick Rauter, Yi Song, Jing Kong, Marko Loncar, and Federico Capasso. High-responsivity mid-infrared graphene detectors with antenna-enhanced photocarrier generation and collection. *Nano letters*, 14(7):3749–3754, 2014.
- [64] Hongtao Yuan, Hidekazu Shimotani, Atsushi Tsukazaki, Akira Ohtomo, Masashi Kawasaki, and Yoshihiro Iwasa. High-density carrier accumulation in zno field-effect transistors gated by electric double layers of ionic liquids. *Advanced Functional Materials*, 19(7):1046–1053, 2009.
- [65] TR Zhan, FY Zhao, XH Hu, XH Liu, and J Zi. Band structure of plasmons and optical absorption enhancement in graphene on subwavelength dielectric gratings at infrared frequencies. *Physical Review B*, 86(16):165416, 2012.
- [66] Yuanbo Zhang, Yan-Wen Tan, Horst L Stormer, and Philip Kim. Experimental observation of the quantum hall effect and berry’s phase in graphene. *Nature*, 438(7065):201–204, 2005.
- [67] Xiaolong Zhu, Wei Yan, Peter Uhd Jepsen, Ole Hansen, N Asger Mortensen, and Sanshui Xiao. Experimental observation of plasmons in a graphene monolayer resting on a two-dimensional subwavelength silicon grating. *Applied Physics Letters*, 102(13):131101, 2013.